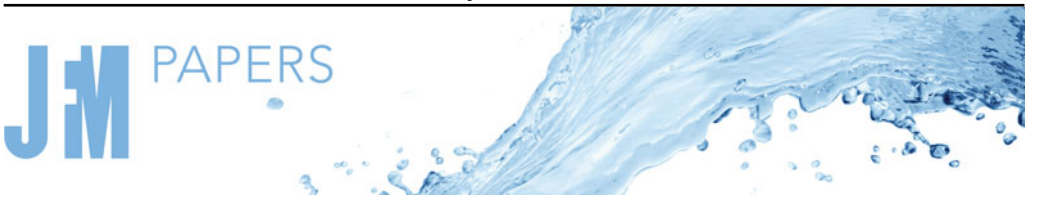
J. Fluid Mech. (2026), *vol.* 1026, A23, doi:10.1017/jfm.2025.11019



Discrete vortex-based broadcast mode analysis for mitigation of dynamic stall

Het D. Patel[1], **Yi Tsung Lee**[1], **Ashok Gopalarathnam**[1] and **Chi-An Yeh**[1]

[1]Department of Mechanical and Aerospace Engineering, North Carolina State University, Raleigh, NC 27695, USA

Corresponding author: Het D. Patel, hdpatel3@ncsu.edu

(Received 17 June 2025; revised 17 October 2025; accepted 2 December 2025)

We integrate a discrete vortex method (DVM) with complex network analysis to strategise dynamic stall mitigation over aerofoils with active flow control. The objective is to inform the actuator placement and the timing to introduce control inputs during the highly transient process of dynamic stall. To this end, we treat a massively separated flow as a network of discrete vortical elements and quantify the interactions among the vortical nodes by tracking the spread of displacement perturbations between each pair of vortical elements using a DVM. This allows us to perform network broadcast mode analysis to identify an optimal set of discrete vortices, the critical timing and the direction to seed perturbations as control inputs. Motivated by the objective of dynamic stall mitigation, the optimality is defined as maximising the reduction of total circulation of the free vortices generated from the leading edge over a prescribed time horizon. We demonstrate the use of the analysis on a two-dimensional flow over a flat plate aerofoil and a three-dimensional turbulent flow over an SD7003 aerofoil. The results from the network analysis reveal that the optimal timing for introducing disturbances occurs slightly after the onset of flow separation, before the shear layer rolls up and forms the core of the dynamic stall vortex. The broadcast modes also show that the vortical nodes along the shear layer are optimal for introducing disturbances, hence providing guidance to actuator placement. Leveraging these insights, we perform nonlinear simulations of controlled flows by introducing flow actuation that targets the shear layer slightly after the separation onset. We observe that the network-guided control results in a 21 % and 14 % reduction in peak lift for flows over the flat plate and SD7003 aerofoil, respectively. A corresponding decrease in vorticity injection from the aerofoil surface under the influence of control is observed from simulations, which aligns with the objective of the network broadcast analysis. The study

© The Author(s), 2026. Published by Cambridge University Press. This is an Open Access article, distributed under the terms of the Creative Commons Attribution licence (https://creativecommons.org/licenses/by/4.0/), which permits unrestricted re-use, distribution and reproduction, provided the original article is properly cited.

https://doi.org/10.1017/jfm.2025.11019 Published online by Cambridge University Press

highlights the potential of integrating the DVMs with the network analysis to design an effective active flow control strategy for unsteady aerodynamics.

Key words: flow control, vortex dynamics, separated flows

1. Introduction

Dynamic stall is a critical flow phenomenon that significantly limits the performance of unsteady wings due to large-amplitude fluctuations in lift force beyond the static limit (McCroskey 1981; Carr 1988). This phenomenon is intrinsically linked to the unsteady separation of flow over the wing surface, culminating in the formation of a dynamic stall vortex (DSV) (McCroskey, Carr & McAlister 1976). The DSV is a dominant flow feature of dynamic stall flows, generated by the accumulation of surface vorticity flux concentrated near the leading edge during the wing's motion (Eldredge & Jones 2019). The severe unsteady aerodynamic loads associated with dynamic stall can impose significant performance and structural constraints, underscoring the importance of effective mitigation strategies with active flow control (Karim & Acharya 1994; Greenblatt & Wygnanski 2001; Weaver, McAlister & Tso 2004; Kissing *et al.* 2021).

While active flow control has demonstrated promising capabilities in mitigating dynamic stall, its design can be challenging due to the highly unsteady and transient nature of the flow (Gardner *et al.* 2017; Zhu *et al.* 2022; Gardner *et al.* 2023). Particularly, the transient nature of the flow makes it difficult, yet even crucial, to determine an effective timing and location for control inputs to be introduced. The timing of actuation for dynamic stall flows is unclear due to the intricate interplay between the time scale of the flow dynamics and that of the wing motion (Feszty, Gillies & Vezza 2004; Lombardi, Bowles & Corke 2013; Tadjfar & Asgari 2018; de Souza *et al.* 2025). Such interplay also makes actuator placement a daunting question since it causes the separation point to travel over a great extent of the suction surface (Weaver *et al.* 2004; Post & Corke 2006; Singh *et al.* 2006; Kissing *et al.* 2020). Therefore, there is a critical need for formal theoretic approaches to determine effective timing and location of actuation (Natarajan, Freund & Bodony 2016; Nair *et al.* 2021; Godavarthi, Kawamura & Taira 2023) for mitigating dynamic stall.

Complex network analysis emerges as an appealing tool to address the need, since analogous questions arise in the field of network science (Albert & Barabási 2002; Newman 2010; Iacobello, Ridolfi & Scarsoglio 2021). Determining a location for actuator placement is similar to identifying a hub for disease transmission over a human or animal network (Nande *et al.* 2021; Safari *et al.* 2025). Modulating the timing of introducing control input is also analogous to determining when to implement preventive measures for disease outbreaks, such as social distancing and isolation (Schlosser *et al.* 2020; Vinceti *et al.* 2020). Therefore, not only does network science offer a broad and mature set of tools to address the aforementioned challenges for flow control (Sujith & Unni 2020; Yeh, Meena & Taira 2021), but its use by the fluid dynamics community has also been witnessed in a growing number of studies, including model reduction (Kaiser *et al.* 2014), force prediction (Iacobello, Kaiser & Rival 2022) and analysing turbulent interactions (Iacobello *et al.* 2019; Li *et al.* 2021; Tandon & Sujith 2023).

Constructing a network model requires the definitions of nodes and edge weights that quantify the interactions between the nodes. Following the classic perspective in

https://doi.org/10.1017/jfm.2025.11019 Published online by Cambridge University Press

aerodynamics where fluid flows can be modelled as an ensemble of discrete vortices (Katz 1981; Saffman 1995; Anderson 2016), vortical elements have been adopted by many fluid dynamics studies as the nodes of fluid networks (Lander & Holland 1993; Bai *et al.* 2019; Meena & Taira 2021). To quantify the interactions between the vortical nodes, discrete vortex methods (DVMs) (Cottet & Koumoutsakos 2000; Eldredge 2007; Eldredge, Wang & Michael 2009) become a natural choice due to their extensive applications to aerodynamic studies (Ramesh *et al.* 2014; SureshBabu, Ramesh & Gopalarathnam 2019; Alvarez & Ning 2020; Herndon & Jaworski 2023). In general, DVMs model a flow by time evolving the locations of discrete vortices in a Lagrangian manner. Building on this idea, Ansari, Żbikowski & Knowles (2006) demonstrated that DVMs can effectively capture the wake dynamics and unsteady aerodynamic forces on an impulsively started flat plate. The work of Eldredge (2007) developed a DVM to model the flow around an unsteady body, formulating the approach based on the principles of vorticity generation and diffusion described by Koumoutsakos, Leonard & Pepin (1994). The DVM framework was later improved by Xia & Mohseni (2013), who enforced a Kutta condition at the leading edge for high angles of attack and relaxed this condition at lower angles to accurately model the leading-edge flow over a pitching flat plate. Subsequent improvements have further expanded the applicability of DVMs to more complex flows (Xia & Mohseni 2017; Darakananda & Eldredge 2019; Dumoulin, Eldredge & Chatelain 2023).

In general, DVMs model unsteady aerodynamic flows by introducing new vortical elements into the flow while determining their circulation strength upon formation (Clements 1973; Sarpkaya 1975; Ramesh *et al.* 2014). Such introduction of finite-circulation vortices into the flow can be translated to vorticity injection that accounts for the formation of a DSV. Thus, in the context of DVMs, the objective of dynamic stall mitigation can be realised by modulating the strength of discrete vortices introduced to the flow, and such modulation can be achieved by perturbing the vortical elements present in the flow. Also, through an objective-informed combination of the DVM and vortical network analysis, the effective timing and location of actuation can be identified by finding a critical set of vortical nodes at which an introduced perturbation at the identified timing can result in a high level of modification in vorticity injection.

In this study we present a DVM-based network analysis to guide the timing, location and direction of actuation for mitigating dynamic stall. To this end, we model the dynamic stall flow as a time-varying network of discrete vortices and use a DVM (Ramesh *et al.* 2014; Lee *et al.* 2022) to extract the interactions between the vortical nodes, as shown in figure 1. Motivated by the objective of flow control, we quantify these vortical interactions (edge weights) by tracking the spread of displacement perturbations between the vortical elements with the use of the DVM. Moreover, this integration of the DVM and network analysis allows us to recast the questions of actuation timing, direction and actuator location into an optimisation problem that seeks an optimal set of vortical nodes to perturb and the timing to perturb them in a direction such that vorticity injection is minimised during dynamic stall and, hence, lift fluctuations can be reduced.

With such an integration of the DVM and network analysis, this study extends the broadcast mode analysis of Yeh *et al.* (2021) in several different aspects. While Yeh *et al.* (2021) considered a set of Eulerian grid points as the vortical nodes, this work directly utilises the Lagrangian vortical elements in the DVM as the nodes of the network. Moreover, motivated by the objective of flow control, the present study quantifies the interactions between the vortical nodes by tracking the spread of displacement perturbation among them. This edge-weight definition distinguishes the present study from Yeh *et al.* (2021) and many previous ones (Nair & Taira 2015; De *et al.* 2023; Wang *et al.* 2025)

https://doi.org/10.1017/jfm.2025.11019 Published online by Cambridge University Press

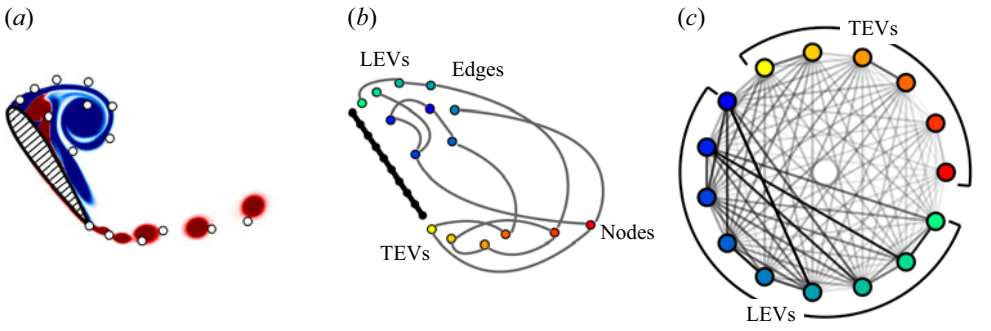


Figure 1. An overview of the present study: (*a*) a flow undergoing dynamic stall is modelled by a DVM (Ramesh *et al.* 2014); (*b*) the vortical elements are treated as network nodes to form a vortical network; (*c*) their interactions are extracted from the DVM as the edge weights to enable network analysis for mitigating dynamic stall. The vortices shown in (*b*) comprise of leading-edge vortices (LEVs) and trailing-edge vortices (TEVs).

that adopted the induced velocity between vortical elements as the edge weights of the vortical networks, according to the Biot–Savart law. The broadcast mode analysis by Yeh *et al.* (2021) used a singular value decomposition to seek the maximum amplification of vortical perturbations for modifying the evolution of two-dimensional (2-D) turbulence by targeting dynamically influential regions. Compared with Yeh *et al.* (2021), this work generalises the analysis by formulating an optimisation problem that seeks a vortical perturbation not only for high amplification, but also in a manner that the identified perturbation maximises the reduction of vorticity injection, given the objective of reducing lift fluctuation by weakening the DSV. Combining with the control-motivated edge weights, such a generalisation of broadcast mode analysis provides insights into the optimal direction of actuation, in addition to identifying dynamically influential regions in the flow for actuator placement. Moreover, it also allows for the identification of effective timing of actuation by considering different time horizons over which the maximum reduction of vorticity injection is sought.

In what follows, we discuss the problem set-up for the dynamic stall flows in § 2. The construction of the DVM-based network model with the goal of guiding circulation control is elaborated in § 3. In § 3.3 we present the broadcast mode analysis (Grindrod & Higham 2014; Yeh *et al.* 2021) to identify the optimal location and timing for actuation with the objective of dynamic stall mitigation by modulating vorticity injection. Section 4 leverages the insights from the analysis to inform flow control design and demonstrates the effectiveness of the network-based approach for mitigating dynamic stall.

2. Problem set-up

We consider two incompressible flows undergoing dynamic stall, as shown in figure 2. The first case (case A) is a flow over a 2-D flat plate aerofoil in pitch-up motion at a chord-based Reynolds number, $Re \equiv u_\infty L_c/\nu_\infty = 1\,000$. Here, u_∞ is the free-stream velocity, L_c is the chord length and ν_∞ is the kinematic viscosity. For this case of pitching aerofoil, the instantaneous angle of attack is prescribed via

$$\alpha(t) = \alpha_0 + \frac{\alpha_f}{b} \ln\left[\frac{\cosh(a(t-t_1))}{\cosh(a(t-t_2))}\right], \tag{2.1}$$

https://doi.org/10.1017/jfm.2025.11019 Published online by Cambridge University Press

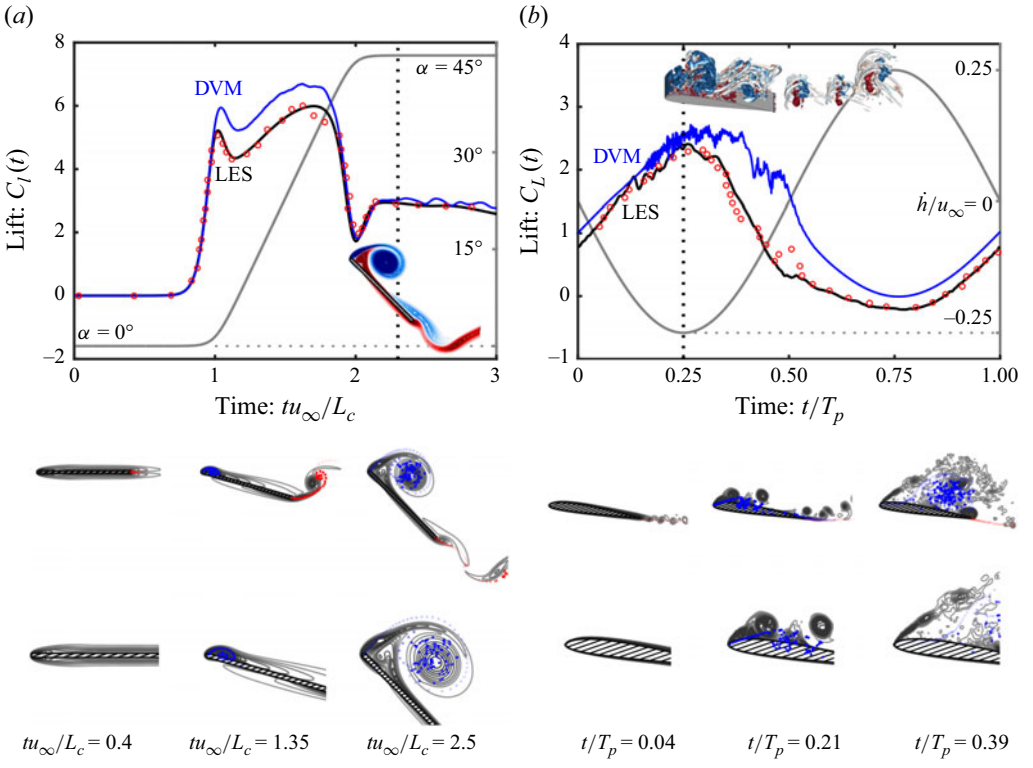


Figure 2. The two dynamic stall flows considered in this study: (*a*) a flow over a pitching flat plate aerofoil (case A) – the red circles (○) are the results by Ramesh *et al.* (2014); (*b*) flow over a periodic heaving-plunging SD7003 aerofoil (case B) – the red circles (○) are the results by Visbal (2011). Contour lines of spanwise vorticity $\omega_z L_c/u_\infty \in [-20, 20]$ is shown for case (*a*). Isosurface of $QL_c^2/u_\infty^2 = 80$ coloured by spanwise vorticity is shown for case (*b*). Motion parameters in (2.1) for case A: $\alpha_0 = \alpha_f = 22.5°$, $aL_c/u_\infty = 11$, $b = 10.78$, $[t_1,\ t_2]/(L_c/u_\infty) = [1,\ 1.98]$; motion parameters in (2.2) for case B: $v_0/u_\infty = 0.25$, $T_p u_\infty/L_c = 4\pi$. The DVM states at key instants are overlaid on the contour lines of spanwise vorticity for comparison. In the DVM, blue circles (●) indicate LEVs and red circles (●) indicate TEVs. The close-up view for these key instances are presented to highlight the comparison of leading-edge flow between DVM and CFD. For the DVM states, the circulation strength of discrete vortices is indicated by transparency – the lower the circulation strength, the greater the transparency, and *vice versa*.

following Eldredge *et al.* (2009) and Ramesh *et al.* (2014). We consider this pitch-up and hold motion, since the onset of dynamic stall occurs during the pitch-up process, and the flow exhibits rich physics involving the formation and convection of the DSV. The second case (case B) is a spanwise-periodic three-dimensional (3-D) turbulent flow over an SD7003 aerofoil undergoing periodic heaving-plunging motion at $Re = 60\,000$, where the instantaneous vertical velocity of the aerofoil is given by

$$\dot{h}(t) = -v_0 \sin\left(2\pi t/T_p\right), \tag{2.2}$$

following Visbal (2011), Ramos *et al.* (2019). The motion parameters in (2.1) and (2.2) are provided in the caption of figure 2, along with the motion profiles, instantaneous lift coefficients and flow visualisations at instants of the DSV departure for both cases.

Baseline (uncontrolled) flows of both cases are obtained using large-eddy simulations (LES) and the DVM. The LES are performed using the incompressible flow solver package, CharLES (Khalighi *et al.* 2011; Brès *et al.* 2017). This solver uses a node-based,

https://doi.org/10.1017/jfm.2025.11019 Published online by Cambridge University Press

second-order finite-volume method for spatial discretisation and a fractional-step scheme for time stepping. To account for the unsteady motions of the aerofoil, a time-dependent fictitious forcing is added to the right-hand side of the momentum equation (Kim & Choi 2006). Further details about the LES solver, governing equations and computational meshes are provided in Appendix A.

The DVM developed by Ramesh *et al.* (2014) and Lee *et al.* (2022) is employed in the present study. It models unsteady flows over aerofoils by introducing discrete point vortices into the flow, whose circulations are modulated by an empirical leading-edge suction parameter. The time integration of the DVM adopts a fourth-order Runge–Kutta scheme, with a time step $\Delta t u_\infty / L_c = 0.01$. The comparisons in lift obtained from the DVM and LES are also shown in figure 2. Although over-predictions in the DVM lift are seen in both cases, we observe qualitative agreements in their temporal profiles. Quantitatively, the levels of agreement in lift between the DVM and computational fluid dynamics (CFD) are also similar to those reported in previous studies (Ramesh *et al.* 2014; Lee *et al.* 2022). The DVM states at representative instants are also shown on top of the spanwise vorticity fields obtained from the flow simulations. We observe that the onset of the DSV core formation, which occurs at $t u_\infty / L_c = 1.35$ for the flat plate aerofoil and $t/T_p = 0.21$ for the SD7003 aerofoil, is captured in agreement with the flow simulations. For the plunging SD7003 case, the over-prediction in lift by the DVM for $t/T_p > 0.25$ can be attributed to the DSV that is located closer to the aerofoil, compared with that in the flow simulation. The results of the DVM base flow will be used to construct the network model of discrete vortices, which is to be detailed in the following section.

3. Construction of the discrete vortex network

Our goal of mitigating dynamic stall is approached by modelling the stall flows as networks of vortical elements, which enables a control-focused network analysis to provide guidance to effective actuation timing, location and direction. The first step of the network analysis is to construct an adjacency matrix, $\boldsymbol{A}$, with each of its entries, A_{ij}, representing a quantifiable interaction (edge weight) between a pair of vortical nodes i and j. Below, we discuss how these vortical interactions are quantified with the use of a DVM.

3.1. *The discrete vortex method*

Here, we provide a concise overview of the DVM developed by Ramesh *et al.* (2014) and Lee *et al.* (2022), which is employed in this study to quantify the interactions between the vortical nodes. Although some details below may be specific to the adopted DVM, our discussion will emphasise how it facilitates the construction of the vortical network in a manner that the general concept is applicable to any DVMs (Cottet & Koumoutsakos 2000; Eldredge 2007). For more details about the DVM, the readers are referred to the original works by Ramesh *et al.* (2014) and Lee *et al.* (2022).

The DVM simulates 2-D flows over an aerofoil using three types of discrete vortices: leading-edge vortices (LEVs), trailing-edge vortices (TEVs) and bound vortices (BVs), as illustrated in figure 3. The BVs are distributed along the mean camber line of the aerofoil and represent its location. The LEVs represent the flow separated from the leading edge of the aerofoil and the TEVs capture the flow past the trailing edge. Together, LEVs and TEVs are referred to as free vortices (FVs), since their locations vary in time. Here, we denote the locations and circulations of all FVs at time $t = t_k$ by

$$\boldsymbol{\Xi}_k^{fv} = \left[\boldsymbol{\xi}_{1,k}^{fv},\ \boldsymbol{\xi}_{2,k}^{fv},\ \ldots,\ \boldsymbol{\xi}_{n_{fv},k}^{fv}\right] \quad \text{and} \quad \boldsymbol{\Gamma}_k^{fv} = \left[\gamma_1^{fv},\ \gamma_2^{fv},\ \ldots,\ \gamma_{n_{fv}}^{fv}\right], \tag{3.1}$$

https://doi.org/10.1017/jfm.2025.11019 Published online by Cambridge University Press

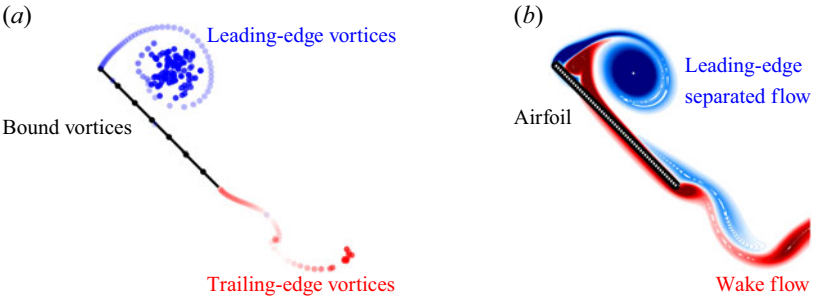


Figure 3. The flow state in DVM is illustrated in (*a*) with arrangement of bound, trailing-edge and leading-edge vortical elements and its comparison with an actual flow simulation is presented in (*b*).

where n_{fv} is the number of FVs present in the flow at t_k. Note that n_{fv} increases in time, i.e. $n_{fv} = n_{fv}(t)$, since the DVM introduces new FVs to the flow at every time step. Also, once a FV is introduced to the flow, its circulation is held constant in time; therefore, the time index k is not needed for γ^{fv} values. Similarly, the circulations of the BVs at $t = t_k$ are denoted by

$$\boldsymbol{\Gamma}^{bv}_k = \left[\gamma^{bv}_{1,k},\ \gamma^{bv}_{2,k},\ \ldots,\ \gamma^{bv}_{n_{bv},k}\right], \tag{3.2}$$

where n_{bv} is the number of BVs distributed along the aerofoil. We also note that the locations of the BVs, $[\boldsymbol{\xi}^{bv}_{1,k},\ \boldsymbol{\xi}^{bv}_{2,k},\ \ldots,\ \boldsymbol{\xi}^{bv}_{n_{bv},k}]$, are given by a prescribed motion of the aerofoil and, hence, are not the state variables to be determined by the DVM.

For each time step from t_k, the DVM seeds a TEV and a LEV, respectively, at the trailing edge ($\boldsymbol{\xi}^{tev}_k$) and leading edge ($\boldsymbol{\xi}^{lev}_k$). (In practice, the introduction of a LEV at a given instant is conditioned by the instantaneous leading-edge suction parameter (Ramesh *et al.* 2014). However, for an instant where a LEV is not introduced, this can be alternatively viewed as introducing a null LEV with zero circulation without loss of generality.) The circulations of the newly seeded TEV and LEV, denoted respectively as γ^{tev}_{k+1} and γ^{lev}_{k+1}, are determined along with the circulations of all BVs, $\boldsymbol{\Gamma}^{bv}_{k+1}$, by imposing the no-penetration condition over the aerofoil and Kelvin's circulation theorem. The new TEV and LEV are appended to the state vectors of FVs such that $\boldsymbol{\Xi}^{fv}_{k'} = [\boldsymbol{\Xi}^{fv}_k,\ \boldsymbol{\xi}^{tev}_k,\ \boldsymbol{\xi}^{lev}_k]$ and $\boldsymbol{\Gamma}^{fv}_{k'} = [\boldsymbol{\Gamma}^{fv}_k,\ \gamma^{tev}_{k+1},\ \gamma^{lev}_{k+1}]$, thereby increasing the number of FVs by 2. With the circulations for all BVs and new FVs determined, the DVM then updates the locations of all FVs in $\boldsymbol{\Xi}^{fv}_{k'}$ by

$$\boldsymbol{\xi}^{fv}_{i,k+1} = \boldsymbol{\xi}^{fv}_{i,k} + \Delta t \dot{\boldsymbol{\xi}}^{fv}_{i,k} \quad \text{for all } i = 1,\ 2,\ \ldots,\ n_{fv}(t_k) + 2, \tag{3.3}$$

where Δt is the time increment between t_k and t_{k+1}, and $\dot{\boldsymbol{\xi}}^{fv}_{i,k}$ is the velocity of the ith FV induced by all other discrete vortices. This induced velocity is given by

$$\dot{\boldsymbol{\xi}}^{fv}_{i,k} = \sum_{j=1}^{n_{fv}+2} \mathcal{V}_{bs}\left(\boldsymbol{\xi}^{fv}_{i,k},\ \boldsymbol{\xi}^{fv}_{j,k},\ \gamma^{fv}_j\right) + \sum_{j=1}^{n_{bv}} \mathcal{V}_{bs}\left(\boldsymbol{\xi}^{fv}_{i,k},\ \boldsymbol{\xi}^{bv}_{j,k+1},\ \gamma^{bv}_{j,k+1}\right), \tag{3.4}$$

where $\mathcal{V}_{bs}$ is the Biot–Savart operator written as

$$\mathcal{V}_{bs}\left(\boldsymbol{\xi}_i,\ \boldsymbol{\xi}_j,\ \gamma_j\right) = \frac{\gamma_j}{2\pi} \frac{\hat{\boldsymbol{e}}_z \times (\boldsymbol{\xi}_i - \boldsymbol{\xi}_j)}{|\boldsymbol{\xi}_i - \boldsymbol{\xi}_j|^2 + r_c^2}, \tag{3.5}$$

https://doi.org/10.1017/jfm.2025.11019 Published online by Cambridge University Press

with the core size $r_c = 1.3\Delta t u_\infty$ (Lee *et al.* 2022). Once the locations of all FVs are updated, we obtain $\boldsymbol{\Xi}^{fv}_{k+1} = [\boldsymbol{\xi}^{fv}_{1,k+1},\ \boldsymbol{\xi}^{fv}_{2,k+1},\ \ldots,\ \boldsymbol{\xi}^{fv}_{n_{fv}(t_k),k+1},\ \boldsymbol{\xi}^{tev}_{k+1},\ \boldsymbol{\xi}^{lev}_{k+1}]$, and the time iteration of the DVM is concluded with $\boldsymbol{\Xi}^{fv}_{k+1}$, $\boldsymbol{\Gamma}^{fv}_{k+1} = \boldsymbol{\Gamma}^{fv}_{k'} = [\boldsymbol{\Gamma}^{fv}_{k},\ \gamma^{tev}_{k+1},\ \gamma^{lev}_{k+1}]$ and $\boldsymbol{\Gamma}^{bv}_{k+1}$. Summarising the discussion above, we can express the time-stepping operation of the DVM in brief as

$$\left[\boldsymbol{\Xi}^{fv}_{k+1},\ \gamma^{tev}_{k+1},\ \gamma^{lev}_{k+1},\ \boldsymbol{\Gamma}^{bv}_{k+1}\right] = \mathcal{N}\left(\boldsymbol{\Xi}^{fv}_{k},\ \boldsymbol{\Gamma}^{fv}_{k}\right), \tag{3.6}$$

where $\mathcal{N}$ can be viewed as the discrete-time nonlinear state propagator of the DVM, whose nonlinearity stems from that in the Biot–Savart law.

Observing (3.6), we make a few important notes on how the DVM can be integrated with network analysis to strategise dynamic stall mitigation: first, (3.6) suggests that the circulation introduced from the leading edge (γ^{lev}_{k+1}) can be modified by perturbing the locations of FVs ($\boldsymbol{\Xi}^{fv}_{k}$) present in the flow; second, if the location of a FV is perturbed at a time instant, the locations of all FVs will be perturbed at all future instants successively, resulting in continuous modification in the circulation introduced from the leading edge. Since this circulation introduction can be translated to a concentrated vorticity injection from the leading edge, which results in the formation of a DSV, (3.6) also implies that dynamic stall mitigation can be potentially achieved by perturbing the FVs in the flow. Thus, the objective of the network analysis is to identify a set of FVs and an effective timing at which introduced perturbations to their locations can result in favourable modifications to the circulations of LEVs. Below, we discuss how this objective can be achieved by appropriately quantifying the interactions between the vortical elements.

3.2. *The time-evolving vortical network: adjacency and communicability matrices*

Motivated by the observations on (3.6), we treat FVs in the DVM as the nodes in our network analysis. To quantify the interactions between them, we focus on those that take place due to displacement perturbations introduced to the vortical nodes, since such perturbations result in a continuous change in the circulation introduced from the leading edge.

In this study we construct the adjacency matrix by measuring the displacement perturbation passed between a pair of vortical nodes. Given *a priori* an instantaneous FV state at t_k where $\boldsymbol{\Xi}^{fv}_{k}$ and $\boldsymbol{\Gamma}^{fv}_{k}$ are known, we define the edge weight, $A_{ij,k}$, as the resulting displacement of vortical node i over a time increment due to a small displacement perturbation introduced to vortical node j. That is,

$$A_{ij,k} = \frac{\partial \boldsymbol{\xi}^{fv}_{i,k+1}}{\partial \boldsymbol{\xi}^{fv}_{j,k}}. \tag{3.7}$$

Using the state propagator of the DVM (3.6), this edge weight can be computed by

$$A_{ij,k} = \frac{1}{\epsilon}\left[\mathcal{N}\left(\boldsymbol{\Xi}^{fv}_{k} + \epsilon\boldsymbol{\Xi}'(j),\ \boldsymbol{\Gamma}^{fv}_{k}\right) - \mathcal{N}\left(\boldsymbol{\Xi}^{fv}_{k},\ \boldsymbol{\Gamma}^{fv}_{k}\right)\right]\Big|_{\boldsymbol{\xi}^{fv}_{i,k+1}}, \tag{3.8}$$

where $\epsilon\boldsymbol{\Xi}'(j)$ introduces an $\boldsymbol{\epsilon}$ perturbation to the location of the jth FV and zeros for all other FVs. The calculation for edge weights is demonstrated in figure 4. The translation of the ith FV over a time step is changed from $\boldsymbol{\xi}^{fv}_{i,k+1}$ to $\boldsymbol{\xi}'^{fv}_{i,k+1}$ due to an $\boldsymbol{\epsilon}$ perturbation that displaces $\boldsymbol{\xi}^{fv}_{j,k}$ to $\boldsymbol{\xi}'^{fv}_{j,k}$, as shown in figure 4(*b*). Thus, following (3.8), the edge weight, $A_{ij,k}$, is computed by

https://doi.org/10.1017/jfm.2025.11019 Published online by Cambridge University Press

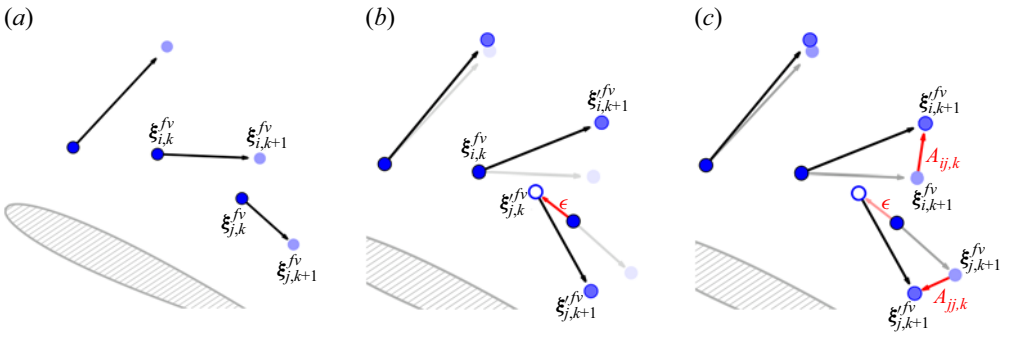


Figure 4. Demonstration of the edge-weight calculation: (*a*) the translations of the ith and jth FVs over a time step without perturbations; (*b*) an $\boldsymbol{\epsilon}$ perturbation is introduced to displace the jth FV and changes the translations of the ith and jth FVs over a time step; (*c*) the edge weight, $A_{ij,k}$, is obtained by calculating the differences between the perturbed and unperturbed translations for all FVs.

$$A_{ij,k} = \frac{1}{|\boldsymbol{\epsilon}|}\left(\boldsymbol{\xi}'^{fv}_{i,k+1} - \boldsymbol{\xi}^{fv}_{i,k+1}\right). \tag{3.9}$$

The value of $|\boldsymbol{\epsilon}|$ is set to $10^{-7}r_c$, where linear convergence of each A_{ij} is observed. We note that, since both $\boldsymbol{\epsilon}$ and $\boldsymbol{\xi}$ are vectors, the resulting $A_{ij,k}$ is in fact a 2-by-2 matrix for the 2-D setting of the present study. More specifically, the $\boldsymbol{\epsilon}$ perturbation introduced to the jth FV is applied independently in the x and y directions. The x-direction perturbation introduced to the jth FV will induce a displacement of the ith FV in both the x and y directions. Likewise, perturbing the same jth FV in the y direction yields the corresponding displacement of the ith FV in both directions. For conceptual simplicity, we refer to the direction-embedded pairwise interaction as the edge weight. Once the edge weights for all pairs of vortical nodes, $A_{ij,k}$, are computed, the adjacency matrix, $\boldsymbol{A}_k \in \mathbb{R}^{2n_{fv}\times 2n_{fv}}$, can be fully constructed with a given $\boldsymbol{\Xi}^{fv}_k$ and $\boldsymbol{\Gamma}^{fv}_k$ at $t = t_k$.

Note that the locations of FVs, $\boldsymbol{\Xi}^{fv}_k$, vary in time. This results in a time-varying vortical network, where the edge weights and the constructed $\boldsymbol{A}_k$ become time dependent. In order to track the perturbation spread over such a network, a communicability matrix is required to account for the time-varying interactions between the vortical nodes (Grindrod & Higham 2013, 2014). The communicability matrix, $\boldsymbol{S}(t_n, t_m)$, describes the interactions between the network nodes that occur over a finite-time horizon from t_n to t_m. To construct $\boldsymbol{S}(t_n, t_m)$, we first collect a series of snapshots for $\boldsymbol{\Xi}^{fv}_k$ and $\boldsymbol{\Gamma}^{fv}_k$ at each time step of the DVM over the time interval $t \in [t_n, t_m]$. These snapshots result in a series of adjacency matrices, $\boldsymbol{A}_k$, where k is the time index of the FV state about which the adjacency matrix is constructed. Then, we follow Grindrod *et al.* (2011) and Grindrod & Higham (2013) to construct the communicability matrix $\boldsymbol{S}(t_n, t_m)$ by recurrently using

$$\boldsymbol{S}(t_n, t_{k+1}) = \left[\boldsymbol{I} + \boldsymbol{A}_k\right]\left[\boldsymbol{I} + e^{-1}\left(\boldsymbol{S}(t_n, t_k) - \boldsymbol{I}\right)\right], \tag{3.10}$$

for $k = n,\ n+1,\ \ldots,\ m-1$, with $\boldsymbol{S}(t_n, t_n) = \boldsymbol{I}$, the identity matrix. In (3.10) the time-downweighting factor, e^{-1}, enforces a finite-time decay of vortical perturbations and suppresses unbounded growth of their magnitudes. This is conceptually similar to the exponential discounting in resolvent analysis (Jovanović 2004; Yeh *et al.* 2020) and can be motivated by the flow hysteresis during dynamic stall, where the memory effect of wing motion eventually diminishes (Corke & Thomas 2015). For the present vortical perturbation network, each entry of the communicability matrix, or S_{ij} of $\boldsymbol{S}(t_n, t_m)$,

https://doi.org/10.1017/jfm.2025.11019 Published online by Cambridge University Press

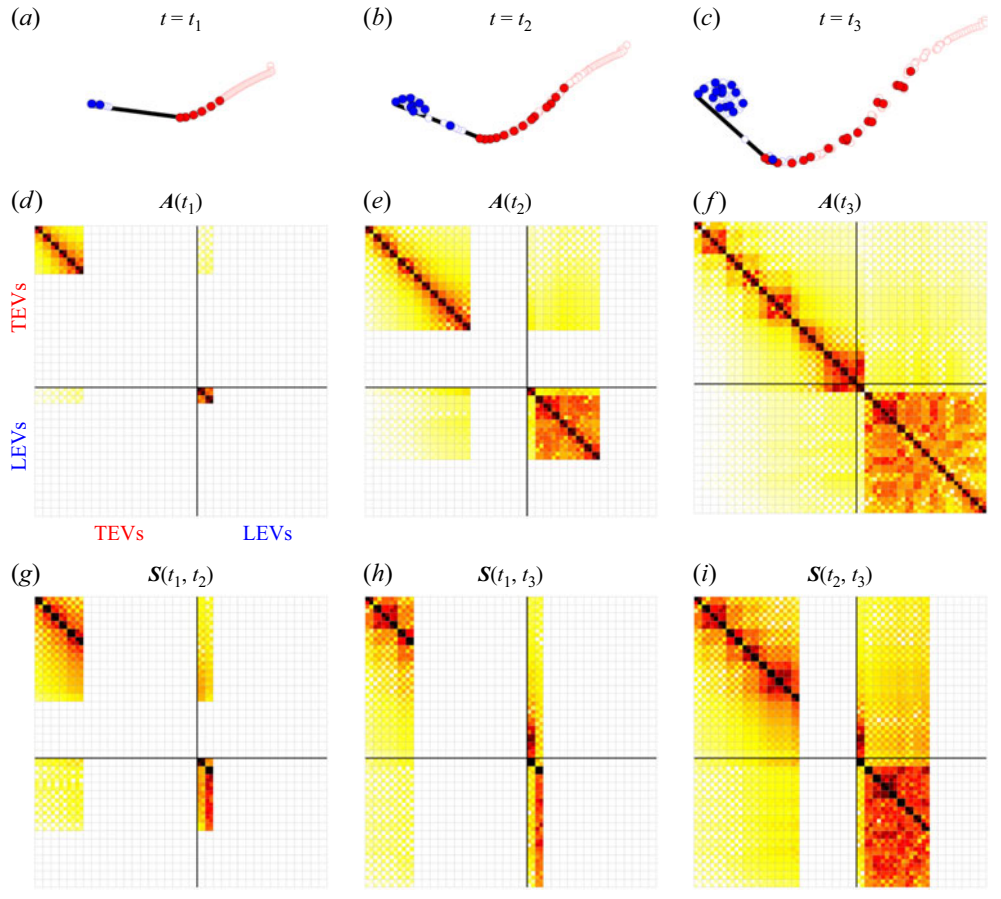


Figure 5. The adjacency and communicability matrices constructed about and between three representative time instances. (*a–c*) Locations of FVs at each instance. (*d–f*) Adjacency matrices constructed about each instance. (*g–i*) Communicability matrices constructed between the combinations of the instances. For visual clarity, the matrices in (*d–i*) are subsampled such that only the interactions between the vortical elements highlighted by solid colours in (*a–c*) are shown.

represents the resulting displacement of the ith vortical node at t_m due to the displacement introduced at the jth vortical node at an earlier time t_n. That is, given a FV displacement perturbation at t_n, $\boldsymbol{\Xi}'_n$, the resulting displacement at t_m, $\boldsymbol{\Xi}'_m$ is related to $\boldsymbol{\Xi}'_n$ by $\boldsymbol{S}(t_n, t_m)$ through

$$\boldsymbol{\Xi}'_m = \boldsymbol{S}(t_n, t_m)\boldsymbol{\Xi}'_n. \tag{3.11}$$

Thus, the communicability matrix, $\boldsymbol{S}(t_n, t_m)$, can be viewed as a state-transition operator of the displacement perturbation of FVs, $\boldsymbol{\Xi}'$, over a finite-time horizon between t_n and t_m.

Let us examine in figure 5 the adjacency and communicability matrices constructed at and between a few representative time instants, respectively. These are accompanied by the instantaneous $\boldsymbol{\Xi}^{fv}$ for the same set of instants. For the adjacency matrices at earlier times, we zero pad the rows and columns corresponding to the vortical nodes that have yet to be seeded into the flow. Also, each matrix is dissected into four blocks according to either TEVs or LEVs the rows and columns are associated with. At the earliest instant t_1, where the LEV introduction is just initiated by the DVM, we observe high levels of intra-community interactions within the TEV and LEV groups from the diagonal blocks

https://doi.org/10.1017/jfm.2025.11019 Published online by Cambridge University Press

of $\boldsymbol{A}(t_1)$. Meanwhile, the off-diagonal blocks reveal weaker inter-community interactions between TEVs and LEVs, which is attributed to the longer distances between the TEVs and LEVs. At $t = t_2$, more LEVs and TEVs are introduced to the flow. Their interactions populate the inactive entries of $\boldsymbol{A}(t_1)$ and emerge in the off-diagonal blocks of $\boldsymbol{A}(t_2)$. Notably, while the interactions in the TEVs-to-TEVs block remain limited to the entries near the diagonal (close neighbours of vortical elements), we observe significantly richer interactions within the LEV community, which can potentially be leveraged to mitigate dynamic stall. Similar observations can be made for $\boldsymbol{A}(t_3)$, at which instant the DVM state is characterised by the formation of a DSV. At this instant, we also observe that a LEV has advected to the trailing edge, which results in high levels of interactions between this LEV and the TEVs just seeded into the flow.

Next, let us move our attention to the communicability matrices constructed between these three representative time instants. Since each S_{ij} element of $\boldsymbol{S}(t_n, t_m)$ represents the displacement of the ith vortex at t_m due to a perturbation introduced to the jth vortex at t_n, the jth column of $\boldsymbol{S}(t_n, t_m)$ represents the resulting displacements of all the vortices present at t_m due to the perturbation of the jth vortex at t_n. Therefore, the columns of non-zero elements in $\boldsymbol{S}(t_n, t_m)$ are the same as those in $\boldsymbol{A}(t_n)$, and the rows of non-zero elements in $\boldsymbol{S}(t_n, t_m)$ are the same as those in $\boldsymbol{A}(t_m)$. Such a structure of $\boldsymbol{S}(t_n, t_m)$ suggests that only the vortical elements present at t_n can be perturbed, and the perturbation can spread to all vortical elements present at t_m. Comparing $\boldsymbol{S}(t_1, t_2)$ with $\boldsymbol{A}(t_1)$, we observe higher levels of interactions in the off-diagonal entries for both intra- and inter-community interactions within and between the TEV and LEV groups, respectively. The same observations can be made by comparing $\boldsymbol{S}(t_1, t_3)$ with $\boldsymbol{A}(t_1)$ and $\boldsymbol{S}(t_2, t_3)$ with $\boldsymbol{A}(t_2)$, which is attributed to the spread of perturbations over time. Similar to $\boldsymbol{A}$, stronger intra-community interactions within the LEV group are observed for $\boldsymbol{S}$. Most importantly, all communicability matrices show stronger LEVs-to-TEVs interactions than TEVs-to-LEVs interactions. This implies that perturbing LEVs is more effective in resulting in a global modification of discrete vortex dynamics compared with perturbing TEVs.

3.3. *The network broadcast analysis*

Recall the remarks we made on the state propagator of the DVM (3.6): it suggests that dynamic stall mitigation can potentially be achieved by identifying a set of FVs and an effective timing at which introduced perturbations result in desirable modifications to the LEV circulations. This motivates the use of network broadcast analysis (Grindrod & Higham 2014; Yeh *et al.* 2021) to identify the optimal timing and the corresponding set of FVs at which introduced perturbations effectively reduce the circulations of the LEVs. In this analysis, the capability of each node in spreading information over a time-varying network is quantified by a broadcast mode, and that of each node in collecting information at a later time is distilled into a receiving mode. Traditionally, the broadcast/receiving modes are obtained from either a column/row sum or a singular value decomposition of the communicability matrix (Grindrod & Higham 2014; Yeh *et al.* 2021). Here, we customise its formulation by focusing on how introduced vortical perturbations result in desirable changes of the flow.

In this study we generalise the network broadcast analysis by formulating an optimisation problem that seeks a set of vortical elements where introduced perturbations minimise the circulation generation from the leading edge over a specified time horizon. Recall that the communicability matrix, $\boldsymbol{S}(t_n, t_k)$, serves as a finite-time state propagator for a displacement perturbation, $\boldsymbol{\Xi}'_n$, over $t \in [t_n, t_k]$, as discussed in (3.11). The resulting displacement perturbation at t_k, or $\boldsymbol{\Xi}'_k$, will result in a change in circulation of the new

https://doi.org/10.1017/jfm.2025.11019 Published online by Cambridge University Press

LEV introduced at t_{k+1}. Therefore, we can relate the change of LEV circulation at t_{k+1}, or $\Delta\gamma^{lev}_{k+1}$, to the displacement perturbation introduced at t_n via a state-space representation, written as

$$\boldsymbol{\Xi}'_k = \boldsymbol{S}(t_n, t_k)\boldsymbol{\Xi}'_n, \tag{3.12a}$$

$$\Delta\gamma^{lev}_{k+1} = \sum_{i=1}^{n_{fv}(t_k)} \boldsymbol{C}_k \boldsymbol{\Xi}'_k, \tag{3.12b}$$

where $\boldsymbol{C}_k$ is a diagonal matrix in which each of its diagonal elements,

$$C_{ii,k} = -\mathrm{sgn}(\gamma^{lev}_{k+1})\frac{\partial\gamma^{lev}_{k+1}}{\partial\boldsymbol{\xi}^{fv}_{i,k}}, \tag{3.13}$$

quantifies the reduction of LEV circulation due to a displacement perturbation introduced at the ith vortical node at t_k. Using the DVM state propagator in (3.6), we can compute these diagonal elements via

$$C_{ii,k} = -\frac{\mathrm{sgn}(\gamma^{lev}_{k+1})}{\epsilon}\left[\mathcal{N}\left(\boldsymbol{\Xi}^{fv}_k + \epsilon\boldsymbol{\Xi}'(i),\ \boldsymbol{\Gamma}^{fv}_k\right) - \mathcal{N}\left(\boldsymbol{\Xi}^{fv}_k,\ \boldsymbol{\Gamma}^{fv}_k\right)\right]\Big|_{\gamma^{lev}_{k+1}}. \tag{3.14}$$

Revisiting (3.12), now we can generalise the network broadcast analysis by solving an optimisation problem

$$\begin{aligned} &\underset{\boldsymbol{\Xi}^b(t_n,t_m)}{\arg\max} \quad \mathcal{J}(\boldsymbol{\Xi}^b) = \sum_{k=n}^{m}\Delta\gamma^{lev}_{k+1} = \sum_{k=n}^{m}\sum_{i=1}^{n_{fv}(t_k)} \boldsymbol{C}_k\boldsymbol{S}(t_n,t_k)\boldsymbol{\Xi}^b, \\ &\text{subject to} \quad ||\boldsymbol{\Xi}^b||_2 = 1, \end{aligned} \tag{3.15}$$

to seek a broadcast mode, $\boldsymbol{\Xi}^b(t_n, t_m)$, as an optimal displacement perturbation introduced to vortical elements at t_n that maximises the sum of the reduction in LEV circulations over all later times until t_m. Meanwhile, the receiving mode, $\boldsymbol{\Xi}^{\mathrm{r}}(t_n, t_m)$, is calculated via

$$\boldsymbol{\Xi}^{\mathrm{r}}(t_n, t_m) = \boldsymbol{C}_k\boldsymbol{S}(t_n, t_m)\boldsymbol{\Xi}^b, \tag{3.16}$$

which quantifies the receptivity of each vortical element present at t_m to the perturbation introduced at t_n in the shape of the broadcast mode, $\boldsymbol{\Xi}^b$, with the objective of resulting in the maximum reduction in LEV circulations. Note that the obtained broadcast mode, $\boldsymbol{\Xi}^b(t_n, t_m)$, is optimal for the chosen time horizon $t \in [t_n, t_m]$. Furthermore, the resulting scalar objective function, $\mathcal{J}(\boldsymbol{\Xi}^b(t_n, t_m))$, corresponds to the total reduction in circulations of LEVs introduced to the flow over $t \in [t_n, t_m]$. Thus, the optimal timing of introducing perturbations can be identified by the perturbation time t_n that results in the maximum value of $\mathcal{J}(\boldsymbol{\Xi}^b(t_n, t_m))$ for a given t_m, which can be set to a critical instant associated with the DSV formation. This is demonstrated in figure 6, where the broadcast analysis is conducted between different combinations of t_n and t_m, with $t_m > t_n$. In particular, we sweep over different values of the perturbation time t_n while keeping t_m at two representative values, as shown in figure 6(*a*). For three representative t_n-t_m combinations, marked as (i), (ii) and (iii), the broadcast and receiving modes are visualised by colouring the FVs present at t_n and t_m, respectively, with the corresponding broadcast/receiving strengths, as quantified by the broadcast/receiving modes. Note that the locations of the FVs of high broadcast strength will provide insights into the location of actuation. Since broadcast modes also contain information about the directions along which the vortices are perturbed to result in the highest reduction of LEV circulation, they can also inform the

https://doi.org/10.1017/jfm.2025.11019 Published online by Cambridge University Press

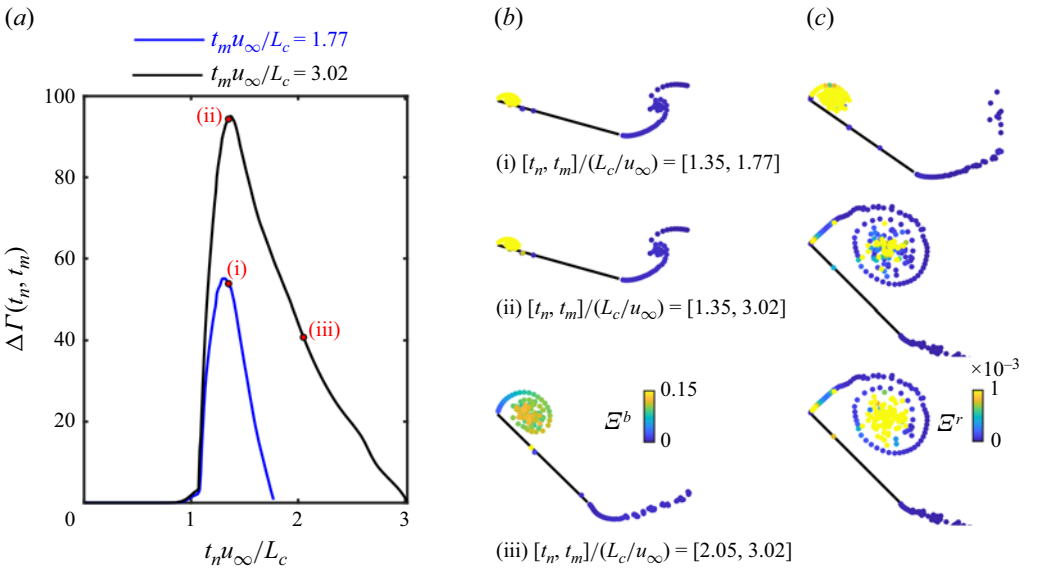


Figure 6. A demonstration of the results of the broadcast mode analysis. The analysis yields three components: (*a*) the total reduction in LEV circulation between t_n (perturbation time) and t_m (a later time); (*b*) the broadcast modes $\boldsymbol{\Xi}^b$, which identify the optimal set of vortical nodes where introduced perturbations result in the highest reduction of LEV circulation; and (*c*) receiving modes $\boldsymbol{\Xi}^r$, which highlight the vortical nodes most influenced by the perturbations originating from the broadcast nodes. Three pairs of $[t_n, t_m]$ are chosen for the visualisation of broadcast and response modes.

design of momentum-based control inputs in nonlinear flows. Moreover, the perturbation time t_n corresponding to high levels of $\Delta\Gamma(t_n, t_m) = \mathcal{J}(\boldsymbol{\Xi}^b(t_n, t_m))$ will be used to guide the timing of introducing control inputs for mitigating dynamic stall. The use of the network broadcast analysis to guide active flow control will be discussed in detail in the next section.

4. Results

4.1. *Baseline flow physics*

To understand the dynamic stall flow physics of the two cases considered, the spanwise vorticity fields at a few representative instants are co-plotted along with the lift coefficients in figure 7. The instantaneous angle of attack and the plunge velocity corresponding to the selected instants are marked along the top horizontal axis for case A (pitching flat plate) and case B (plunging SD7003), respectively. The instantaneous separation point at each instant is also marked by a green dot on the suction side to indicate the flow evolution to leading-edge separation as a signature of dynamic stall (Carr, McAlister & McCroskey 1977; Leishman 1990).

In the beginning of pitching and downstroke motions, respectively, for cases A and B, we observe that the separation point on the suction surface migrates upstream from the trailing edge, as indicated by instants (o) in figures 7(*a*) and 7(*b*). At a later instant (i), leading-edge separation occurs for both cases. At the same time, the stagnation point moves downstream along the pressure side of the aerofoil. Consequently, the flow directed toward the suction surface from the stagnation point negotiates the leading-edge curvature. This accelerates the flow near the leading edge, getting a strong suction force that contributes to a rise in

https://doi.org/10.1017/jfm.2025.11019 Published online by Cambridge University Press

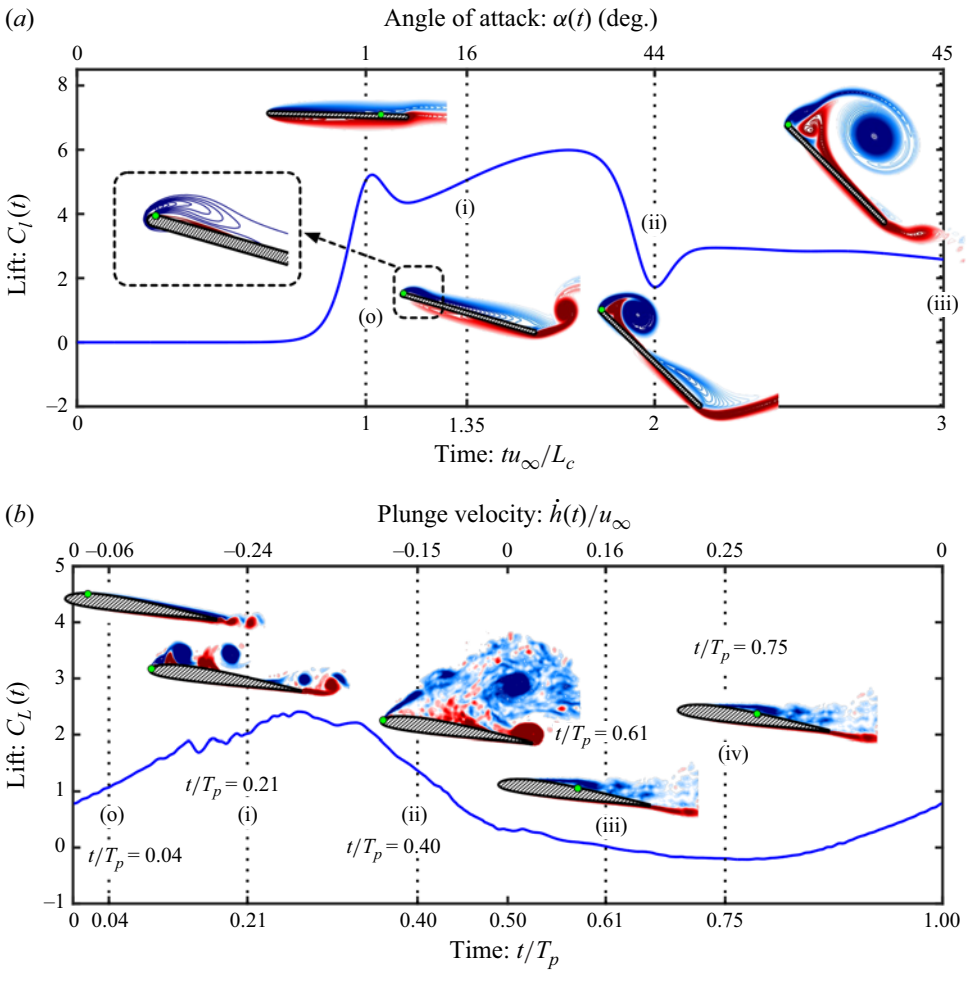


Figure 7. The lift fluctuations for (*a*) case A and (*b*) case B are shown alongside the spanwise vorticity fields at representative time instants. For case A, the close-up view of the flow near the leading edge is presented in the dashed square for $tu_\infty/L_c = 1.35$. For case B, the vorticity fields are averaged in the spanwise direction. The separation point is marked with a green dot (●) in each vorticity field to identify leading-edge separation.

lift force. Moreover, at instant (i) negative vorticity accumulates over the suction surface near the leading edge, which marks the onset of DSV formation (Karim & Acharya 1994). Starting from instant (ii) for case A, the aerofoil is held at $\alpha = 45°$. The separation point remains near the leading edge, while the DSV convects away from the aerofoil surface and results in decreasing lift, as indicated by instants (ii) and (iii) in figure 7(*a*). For case B, the shear layer rolls up into smaller vortices due to the Kelvin–Helmholtz instability (Visbal 2011; Ramos *et al.* 2019). These vortices subsequently coalesce into the DSV, which is visible at instant (ii) in figure 7(*b*). As the DSV departs from the aerofoil surface, a reduction in the lift force from its peak value is observed. During the upstroke phase ($t/T_p \in [0.5, 1]$) for case B, the DSV passes beyond the trailing edge, accompanied by the shift of the separation point downstream along the suction surface. The flow gradually becomes fully attached, as seen at time instants (iii) and (iv) in figure 7(*b*).

From the preceding discussion, it is evident that the formation of the DSV core is preceded by instants (i) in figures 7(*a*) and 7(*b*). This instant captures critical flow features

https://doi.org/10.1017/jfm.2025.11019 Published online by Cambridge University Press

that contribute to the formation of the DSV core and eventually DSV in both cases. For case A, we characterise this instant by shear layer 'pinch-up', where the separated shear layer from the leading edge immediately reattaches to the suction surface at $x/L_c = 0.22$. At this instant, the accumulation of negative vorticity near the leading edge has initiated, which precedes the onset of shear layer roll-up that forms the DSV core. For the turbulent flow case B, the mechanism of DSV core formation differs from that of case A. Here, the shear layer roll-up into spanwise vortices has initiated in the high-Reynolds-number flow, as observed from the instant (i) in figure 7(*b*). Moreover, we observe that the formation of the DSV core is driven by the merging of these spanwise vortices. This instant (i) for both cases marks the onset of DSV core formation, and we will revisit them when discussing the results of the network analysis in the next section.

Since the dynamics of the DSV play a crucial role in the pressure distribution on the aerofoil surface and lift fluctuation, interfering with its formation process by modulating the vorticity injection from the leading edge can hold a key to mitigating dynamic stall. Next, we perform the broadcast mode analysis on the vortical network to identify the effective actuation timing and location, with the goal of achieving effective modulation of vorticity injection to mitigate dynamic stall.

4.2. *Broadcast mode analysis*

As discussed in § 3.3, the network broadcast mode analysis seeks a broadcast mode, $\boldsymbol{\Xi}^b(t_n, t_m)$, as an optimal displacement perturbation introduced to vortical elements at t_n that maximises the reduction in LEV circulations over all later times until t_m. The objective function of the optimisation problem is defined as the sum of the reduction in LEV circulations introduced to the flow over $t \in [t_n, t_m]$ due to a perturbation seeded at t_n. Therefore, the dependency of $\mathcal{J}(\boldsymbol{\Xi}^b(t_n, t_m)) = \Delta\Gamma(t_n, t_m)$ on the time of perturbation, t_n, and the resulting broadcast mode, $\boldsymbol{\Xi}^b(t_n, t_m)$, provide valuable insights into the effective timing and location for flow actuation.

This is shown in figure 8, where the broadcast mode analysis is conducted by sweeping over different combinations of perturbation time t_n and a later time t_m. We obtain the contour plots for $\Delta\Gamma(t_n, t_m)$ below the main diagonal of figures 8(*a*) and 8(*b*), since $t_m > t_n$. Note that the introduction of LEVs in the DVM does not occur until $tu_\infty/L_c = 1.05$ for case A and $t/T_p = 0.11$ for case B. Consequently, the FV states at early times, as represented by instants (o) for both cases, are characterised by the presence of TEVs only. Hence, the broadcast modes at instants (o) are obtained only from these TEV nodes present in the flow. Moreover, the absence of LEVs at early times of perturbation ($t_n u_\infty/L_c < 1.05$ for case A and $t/T_p < 0.11$ for case B) leads to low levels of $\Delta\Gamma$ for both cases. This indicates that introducing perturbations at time instances characterised solely by the presence of TEVs is ineffective in modulating the circulation injected from the leading edge. This can be attributed to the convection of TEVs away from the aerofoil surface that results in low levels of interactions with the aerofoil surface.

Starting from the instants where LEV shedding is initiated, a rapid increase in $\Delta\Gamma$ is observed for both cases. The peaks of $\Delta\Gamma$ occur at perturbation time $t_n u_\infty/L_c = 1.35$ for case A and $t_n/T_p = 0.21$ for case B, both after the initiation of LEV shedding. These peak instants are marked by instants (i) in figures 8(*a*) and 8(*b*). We make an important observation that these specific instants are corresponding to those leading to the DSV core formation, as previously discussed in figure 7. This suggests that the most effective timing of introducing perturbations for reducing LEV circulation corresponds to the early stages of DSV formation. Past instant (i), a decrease in $\Delta\Gamma$ is observed along with the concluded formation of the DSV and its departure from the suction surface. This can be seen at

https://doi.org/10.1017/jfm.2025.11019 Published online by Cambridge University Press

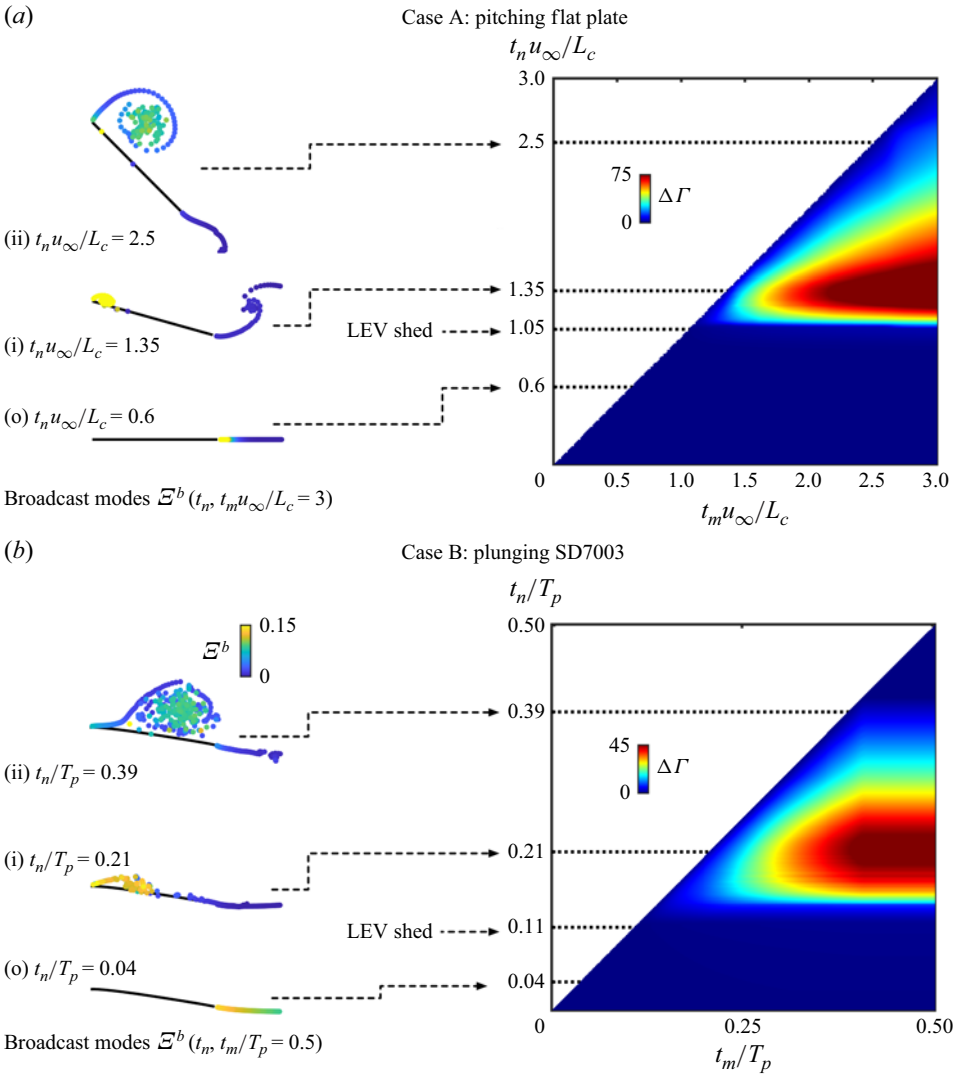


Figure 8. The broadcast mode analyses for case A (*a*) and case B (*b*), sweeping over different combinations of perturbation time t_n and a later time t_m. For both cases, the reduction in LEV circulation, $\Delta\Gamma(t_n, t_m)$, is shown on the right-hand side, and the broadcast modes at three representative instances are visualised on the left-hand side. The broadcast modes are visualised by colouring the corresponding FV nodes by their broadcast strength.

the representative instants (ii) in figures 8(*a*) and 8(*b*) for both cases. At these later time instants, while the DSV continues to accumulate circulations of weaker LEVs, the DSV has become a robust structure and begins to convect away from the aerofoil surface. These observations underscore that once the DSV formation is concluded, the effectiveness of flow perturbation for modulating LEV circulation is significantly reduced.

Let us take a closer look at the $\Delta\Gamma(t_n,\ t_m)$ profiles with respect to different perturbation times (t_n) and a fixed t_m in figure 9. Here, we choose $t_m u_\infty/L_c = 3$ for case A and $t_m/T_p = 0.38$ for case B and extract the $\Delta\Gamma$ values along the constant-t_m lines from figure 8. Note that both of the chosen instants are associated with the concluded formation of the DSV over the suction surface. The resulting trends of $\Delta\Gamma(t_n)$ are shown in figures 9(*a*) and 9(*b*) for case A and case B, respectively. In particular, the broadcast and

https://doi.org/10.1017/jfm.2025.11019 Published online by Cambridge University Press

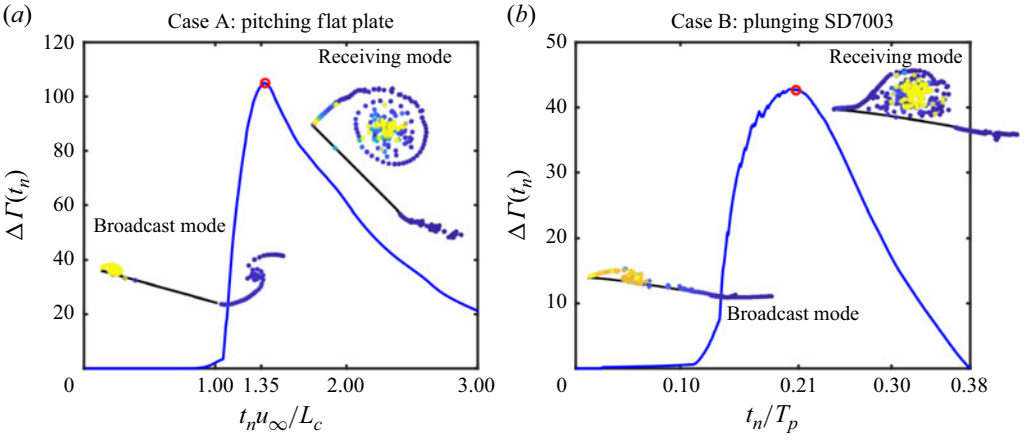


Figure 9. The profiles of $\Delta\Gamma(t_n, t_m)$ for a fixed t_m for (*a*) case A at $t_m u_\infty/L_c = 3$ and (*b*) case B at $t_m/T_p = 0.38$. The peak value of $\Delta\Gamma$ occurs at $t_n u_\infty/L_c = 1.35$ for case A and at $t_n/T_p = 0.21$ for case B, both marked by a red circle (○). The corresponding broadcast and receiving modes are inserted for case A with $[t_n, t_m]/(L_c/u_\infty) = [1.35, 3.00]$ and, for case B, with $[t_n, t_m]/T_p = [0.21, 0.38]$.

receiving modes obtained from the peak t_n, highlighted by a red dot on the $\Delta\Gamma(t_n)$ profile, are also inserted for both cases. Once again, we observe that the broadcast modes, $\boldsymbol{\Xi}^b$, highlight the vortical elements residing along the shear layer emanating from the leading edge. This suggests that perturbations introduced to the shear layer can potentially induce high levels of LEV circulation reduction, as quantified by $\Delta\Gamma$. Moreover, the receiving modes, $\boldsymbol{\Xi}^r$, obtained at the chosen later times t_m, reveal that the LEVs residing within the DSV core are those perturbed the most by the perturbations seeded into the flow at the earlier perturbation time t_n that results in the highest $\Delta\Gamma$. These observations indicate that the optimal timing for introducing perturbations for active flow control occurs slightly after the onset of leading-edge separation and prior to the formation of a DSV core, as identified by the LEV shedding in the DVM. With the identified timing for effective actuation, next we leverage the insights from the broadcast modes to identify an effective location on the aerofoil surface for actuator placement.

Note that the broadcast mode represents the optimal displacement perturbation applied to the Lagrangian vortical nodes. We can translate this Lagrangian perturbation to an Eulerian one by computing the induced velocity perturbation at an Eulerian grid point due to a displacement perturbation introduced at a Lagrangian vortical node by the Biot–Savart operator, $\mathcal{V}_{bs}$, used in the DVM. In this study we aim to place an actuator on the surface of the aerofoil. To this end, we compute the velocity perturbation on the aerofoil surface due to a broadcast mode perturbation via

$$\Delta\boldsymbol{u}(\boldsymbol{x}_s, k) = \sum_{j=1}^{n_{fv}} \left[\mathcal{V}_{bs}\left(\boldsymbol{x}_s,\ \boldsymbol{\xi}^{fv}_{j,k} + \epsilon\boldsymbol{\Xi}^b_{j,k},\ \gamma^{fv}_j\right) - \mathcal{V}_{bs}\left(\boldsymbol{x}_s,\ \boldsymbol{\xi}^{fv}_{j,k},\ \gamma^{fv}_j\right)\right], \tag{4.1}$$

where $\boldsymbol{x}_s$ parametrises a set of Eulerian points on the aerofoil surface at which the velocity perturbation is sought, and the time index k is associated with the time instants where $\Delta\Gamma$ reaches its maximum. This will allow us to choose the actuator locations according to the magnitude of the velocity perturbation, $|\Delta\boldsymbol{u}|$. This is shown in figure 10, where we observe a region near the leading edge that exhibits high levels of $|\Delta\boldsymbol{u}|$ for both cases. This occurs around $x/L_c = 0.02$ from the pitching flat plate (case A) and $x/L_c = 0.04$ for the

https://doi.org/10.1017/jfm.2025.11019 Published online by Cambridge University Press

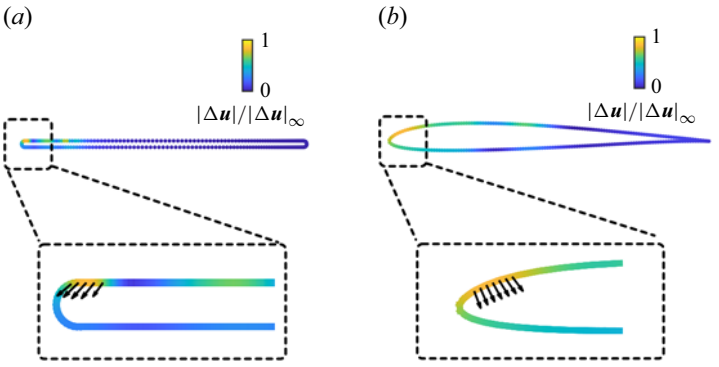


Figure 10. The induced velocity on the aerofoil surface due to the broadcast mode perturbation. The close-up view of the aerofoil section with high magnitude of perturbation velocity, $|\Delta \boldsymbol{u}|$, is presented along with its direction. (*a*) Case A: pitching flat plate and (*b*) Case B: plunging SD7003.

plunging SD7003 (case B), indicating potentially effective locations to introduce control inputs. Moreover, when momentum-based actuators (Cattafesta III & Sheplak 2011) are deployed for flow control, we can also inform the direction of actuation according to the orientation of the velocity perturbation at the peak location. These directions for both cases are also inserted in figures 10(*a*) and 10(*b*) for case A and case B, respectively. Note that the optimal direction shows a combination of both wall-normal and tangential components for both cases.

As a short summary, the broadcast mode analysis provided insights into the effective timing, location and direction for flow actuation. It suggests that applying actuation near the leading edge shortly before the formation of the DSV core can favourably reduce vorticity injection, potentially mitigating dynamic stall. We also note that, due to the use of small perturbation in the construction of the vortical network, the broadcast mode analysis conducted in this section is linear by nature. Although it offers guidance to the effective perturbations that result in a desirable initial departure of the flow states, the long-time nonlinear evolution of the flow under such control inputs needs to be further examined with great care. Therefore, to further interrogate these insights in their effectiveness of reducing the lift fluctuation and vorticity injection, we perform nonlinear flow simulations of the controlled flows, as discussed in the following section.

4.3. *Broadcast mode analysis guided active flow control*

In this section we design active flow control based on the results of broadcast mode analysis and examine its effectiveness in mitigating dynamic stall using LES of controlled flows. Here, we employ a flow actuator (Cattafesta III & Sheplak 2011) on the aerofoil surface, according to the insights obtained from figure 10. This actuator is implemented as a time-varying Dirichlet boundary condition on the aerofoil surface, where the velocity profile is given by

$$\boldsymbol{u}_{act}(\boldsymbol{x}_s, t) = u_{amp} \times g(\boldsymbol{x}_s, \boldsymbol{x}_{act}) \times \phi(t)\, \hat{\boldsymbol{e}}_{act}. \tag{4.2}$$

Here, u_{amp} controls the actuation strength, $g(\boldsymbol{x}_s, \boldsymbol{x}_{act})$ provides a compact spatial support for the actuator placed at $\boldsymbol{x}_{act}$ on the aerofoil surface, $\phi(t)$ controls the temporal duty cycle of the actuation input and $\hat{\boldsymbol{e}}_{act}$ denotes the direction of the momentum-based actuation. The specific forms and parameters for $g(\boldsymbol{x}_s, \boldsymbol{x}_{act})$ and $\phi(t)$ are provided in table 1 for the actuator model:

https://doi.org/10.1017/jfm.2025.11019 Published online by Cambridge University Press

Parameters	Pitching flat plate	Plunging SD7003
t_{on}	$1.29\,L_c/u_\infty$	$0.16\,T_p$
t_{off}	$1.84\,L_c/u_\infty$	$0.39\,T_p$
$\tilde{\nu}$	$80\,L_c/u_\infty$	$10\,T_p$
x_0	$0.02\,L_c$	$0.04\,L_c$
y_0	$0.0115\,L_c$	$0.029\,L_c$
σ	$0.012\,L_c$	$0.012\,L_c$
T^*	$1 L_c/u_\infty$	$1\,T_p$
C_μ	5.5 %	0.04 %

Table 1. The velocity boundary condition for the actuator in the simulation set-up. The analytical forms, parameters and shape for the spatial and temporal profiles of actuation are provided in figures 11(*a*) and 11(*b*), respectively.

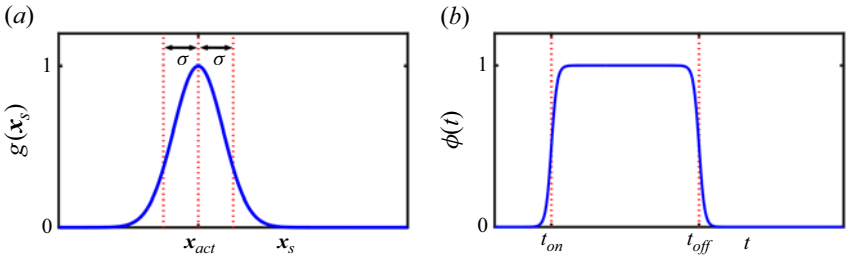


Figure 11. The spatial and temporal profiles of the actuator velocity boundary condition used in the simulation set-up are shown in (*a*) and (*b*), respectively.

$$\text{Actuator model:}\quad \boldsymbol{u}_{act}(\boldsymbol{x}_s, t) = u_{amp} \times \underbrace{\exp\left(-\frac{|\boldsymbol{x}_s - \boldsymbol{x}_{act}|^2}{\sigma^2}\right)}_{g(\boldsymbol{x}_s)} \times \underbrace{\left[\frac{e^{\tilde{\nu}(t-t_{on})}}{1+e^{\tilde{\nu}(t-t_{on})}} - \frac{e^{\tilde{\nu}(t-t_{off})}}{1+e^{\tilde{\nu}(t-t_{off})}}\right]}_{\phi(t)} \hat{\boldsymbol{e}}_{act} \tag{4.3}$$

We leverage the insights from figures 9 and 10 to inform the designs of actuator location, $\boldsymbol{x}_{act}$, actuation direction, $\hat{\boldsymbol{e}}_{act}$, and the temporal profile of actuation, $\phi(t)$. Here, $\boldsymbol{x}_{act}$ is determined according to the location where the induced velocity, $\Delta\boldsymbol{u}$, exhibits the maximum magnitude on the aerofoil surface, as indicated by figure 10. This results in the choices of $\boldsymbol{x}_{act}$ to be 2 %- and 4 %-chord downstream of the leading edge for case A and case B, respectively. The actuation direction, $\hat{\boldsymbol{e}}_{act}$, is also determined in correspondence to the direction of $\Delta\boldsymbol{u}$ at the same hot spot, as indicated by the arrows in figure 10. Lastly, the temporal profile is chosen such that the actuation strength reaches 99 % of its maximum at the optimal timing according to the broadcast mode analysis in figure 9 ($tu_\infty/L_c = 1.35$ for case A and $t/T_p = 0.21$ for case B). We also quantify the actuation input using the momentum coefficient C_μ, defined as

$$C_\mu = \frac{\iint \rho|\boldsymbol{u}_{act}(\boldsymbol{x}_s, t)|\left[\boldsymbol{u}_{act}(\boldsymbol{x}_s, t)\cdot\hat{\boldsymbol{e}}_n(\boldsymbol{x}_s)\right]\mathrm{d}\boldsymbol{x}_s\mathrm{d}t}{\rho_\infty u_\infty^2 L_c T^*}, \tag{4.4}$$

https://doi.org/10.1017/jfm.2025.11019 Published online by Cambridge University Press

where $\hat{\boldsymbol{e}}_n(\boldsymbol{x}_s)$ is the local surface normal vector of the aerofoil and T^* is the time scale of the wing motion. For case A (pitching flat plate), T^* is chosen to be the ramp-up time interval such that $T^* u_\infty / L_c = 1$. For case B (plunging SD7003), T^* is chosen to be the plunging period of the motion, i.e. $T^* = 0.5 T_p$. The momentum coefficients for both cases are also reported in table 1, whose values are chosen in accordance with those reported in previous studies (Chen, Li & Hu 2014; Zigunov, Sellappan & Alvi 2022; Lin, Tsai & Tsai 2023; de Souza *et al.* 2025).

The results of broadcast mode analysis guided flow control for both cases are shown in figures 12 and 13. For both cases, the lift fluctuations in time for baseline and controlled flows are provided with instantaneous flow visualisations at three representative instants. Note that the temporal profiles of control inputs are shown by the shaded regions for both cases. The instantaneous angle of attack and plunge velocity are also shown along the horizontal axis on the top. For both cases, we observe a significant decrease in lift fluctuation. For case A (pitching flat plate), a 21 % reduction in peak lift is observed, as shown in figure 12(*a*). More excitingly, we observe a 14 % decrease in peak lift for the 3-D turbulent flow over the plunging SD7003 aerofoil, as shown in figure 12(*b*). Additionally, a reduction in moment fluctuations is observed in both cases, as shown in figure 13. For case A, a 10.2 % reduction in the moment coefficient is observed around $tu_\infty / L_c = 1.75$. The local negative moment peak at $tu_\infty / L_c = 1.75$ arises from the influence of the DSV, whereas the earlier peak around $tu_\infty / L_c = 1$ is attributed to the added-mass effects. Furthermore, the 13.2 % reduction in peak moment coefficient observed for case B (figure 13) is achieved. These reductions in lift and moment fluctuations for both cases suggest mitigation of dynamic stall using the broadcast mode analysis guided flow control.

In addition to the successful reduction of lift fluctuations achieved by the analysis guided flow control, the flow visualisations inserted in figure 12 also show that the physical mechanism that results in these reductions agrees with the ideation of the broadcast mode analysis and the insights of receiving modes. Flow modifications can be observed starting from instants (i) for both cases, which mark the optimal timings indicated by the broadcast mode analysis. At instants (i) for both cases, we observe that the flow physics near the leading edge are significantly disrupted by the control inputs. This is particularly clear in the visualisations for case A, where we observe that the leading-edge separation at instant (i) ($tu_\infty u / L_c = 1.35$) is effectively suppressed in the controlled flow. This critical modification interferes with the formation process of the DSV core. This is evident at instant (ii) ($tu_\infty u / L_c = 1.75$) in figure 12(*a*). At this instant, a DSV has formed near the leading edge in the baseline flow. However, in the controlled flow we observe that the vorticity accumulated near the leading edge at instant (i) continues to convect along the suction surface and forms a small vortex near the mid-chord at instant (ii). This is evident from figure 12(*a*), where the small vortex formed by accumulated vorticity in the controlled flow is marked by a circle. Moreover, this small vortex does not develop into the DSV observed at instant (iii). Instead, the DSV at instant (iii) is developed by accumulating the vorticity in between the leading edge and the small vortex at instant (ii). These observations indicate that the control input interferes with the DSV formation by dividing the accumulated vorticity into two vortical structures. Notably, instant (ii) is also the instant where the lift reaches its maximum value. For instant (iv) at $tu_\infty / L_c = 2.2$, the formations of the DSV are concluded for both baseline and controlled flows. At this instant, we observe a significantly smaller DSV in the controlled flow, suggesting that the reduction in lift fluctuation is indeed achieved by the modification of the formation process of the DSV.

Similar observations can be made for case B (plunging SD7003) presented in figure 12(*b*). For this high-Reynolds-number 3-D turbulent flow, the control input disrupts

https://doi.org/10.1017/jfm.2025.11019 Published online by Cambridge University Press

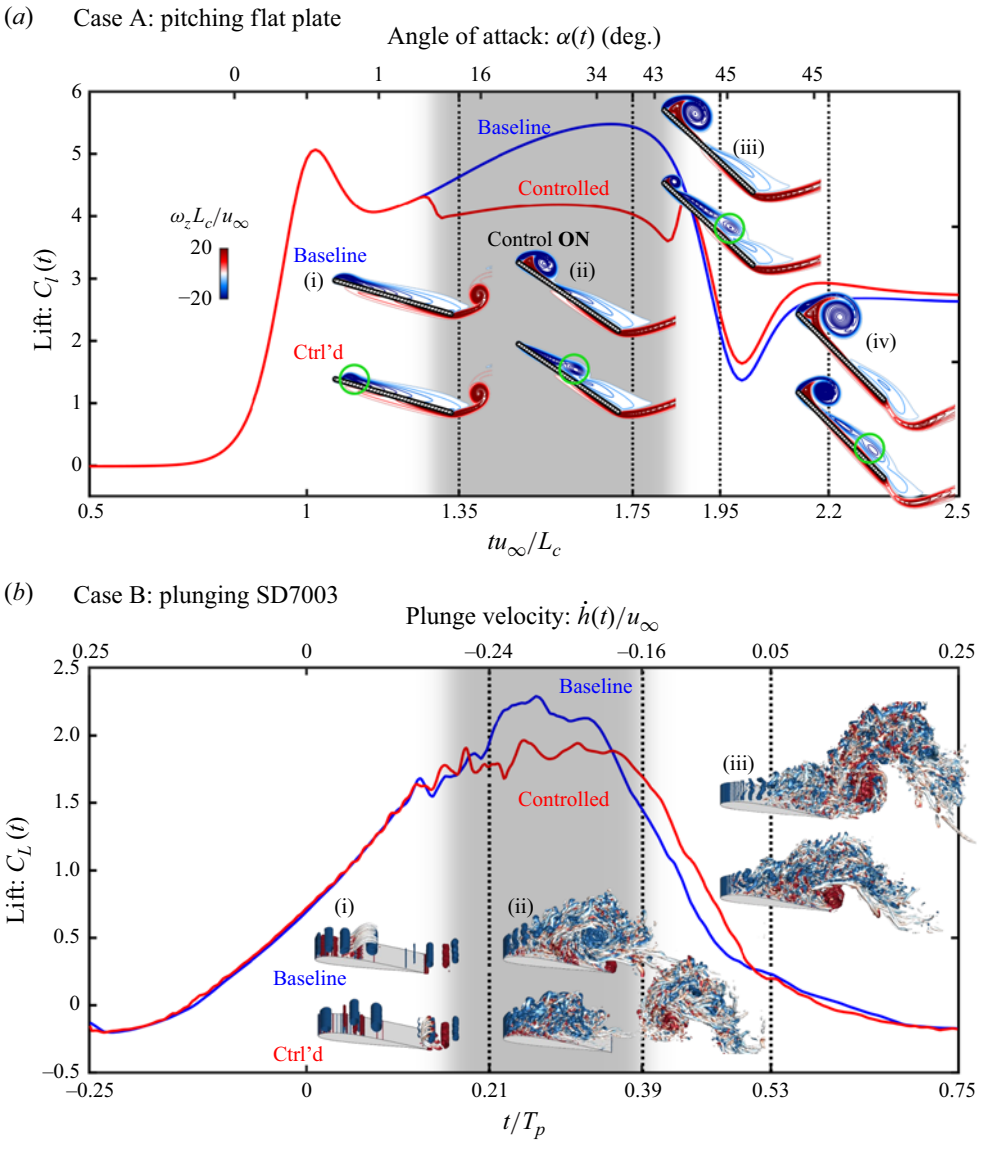


Figure 12. Comparison of lift fluctuations between the baseline and controlled flows for (*a*) case A and (*b*) case B. The spanwise vorticity fields for case A and the Q isosurface coloured by spanwise vorticity for case B are provided at representative time instants for both baseline and controlled flows. For case A, a vortical structure in the controlled flow is highlighted by a green circle (○) to illustrate its evolution. For case B, the lift coefficient, $C_L(t)$, for both the baseline and control cases is cycle averaged over four periods of heaving-plunging motion.

both the roll-up and vortex merging processes, as indicated at instant (i) ($t/T_p = 0.21$). In the baseline flow, the spanwise vortical structures developed from the shear layer roll-up coalesce and form the DSV core. In the controlled flow the shear layer rolls into smaller vortical structures over the suction surface. Moreover, we observe that the control inputs discourage the spanwise rollers from immediately merging and forming the DSV core. Instead, these spanwise vortices continue to convect downstream past the trailing edge. As a consequence, the formation of the DSV core is postponed due to the control input, similar to what we observed in case A. In particular, the DSV in the control flow

https://doi.org/10.1017/jfm.2025.11019 Published online by Cambridge University Press

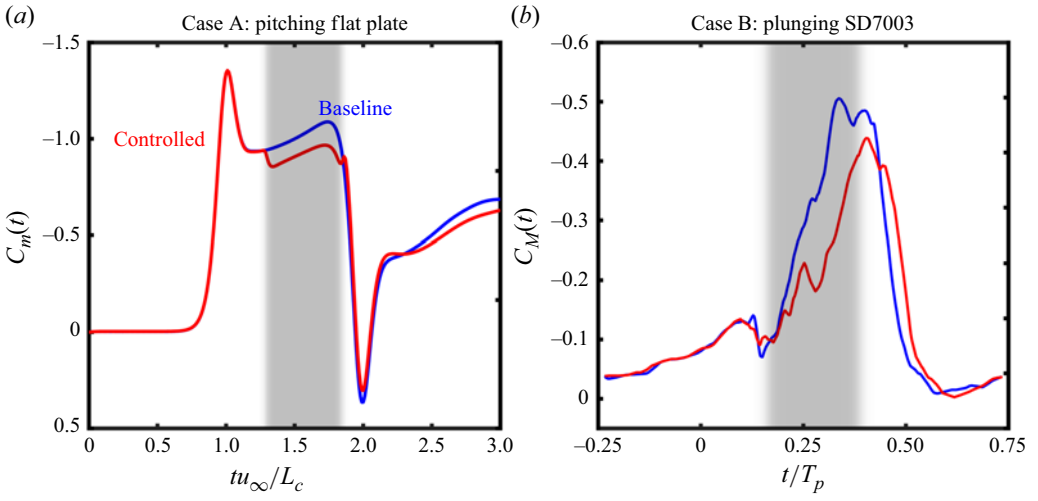


Figure 13. Comparison of the z direction moment fluctuations, computed about the quarter chord, between baseline and controlled flows for (*a*) case A and (*b*) case B. For case B, the moment coefficient $C_M(t)$ for both the baseline and controlled flow is cycle averaged over four periods of heaving-plunging motion.

observed at instant (ii) ($t/T_p = 0.39$) forms from the breakdown of the leading-edge flow into turbulent structures, bypassing the merging process between laminar spanwise rollers in the baseline flow. The DSV at instant (ii) also shows a smaller size in the controlled flow compared with that in the baseline. The strong DSV in the baseline flow triggers the formation of a coherent TEV of positive vorticity, which is not observed in the controlled flow until instant (iii). At instant (iii), we observe the departure of the DSV from the aerofoil surface in the baseline flow. Following the DSV departure, gradual flow reattachment is observed during the upstroke motion. For the controlled flow, the higher lift after $t/T_p = 0.39$ than the baseline flow can be attributed to the delayed DSV departure due to its delayed formation.

The modified DSV dynamics leaves a clear signature in the suction-surface pressure distribution, which leads to the change in lift fluctuation. This is shown in figure 14, where the temporal evolution of the suction-surface pressure distribution (C_p) for the baseline flows and the change in the suction-surface pressure distribution (ΔC_p) for the controlled flows are shown for both cases. For case A, the baseline flow at $tu_\infty/L_c = 1.35$, marked as (i) in figure 14(*a*), exhibits a suction peak near the leading edge. This is the same time instant corresponding to the shear layer pinch-up instant, also marked as (i) in figure 12(*a*). This suction results from the accelerated flow around the leading edge directed from the stagnation point on the bottom surface of the aerofoil. The suction region progressively expands over the suction surface, particularly in the region $x/L_c < 0.3$ during the interval $tu_\infty/L_c < 2$, coinciding with the DSV formation above the suction surface. This suction induced by the formation of the DSV is modified in the controlled flow, as indicated in figure 14(*b*). Downstream of the actuator region, a positive ΔC_p indicates the pressure recovery, which leads to the reduction in lift. This recovery is related to both the delayed formation of the DSV and also its weaker strength.

We observe similar patterns for the suction-surface pressure distribution for case B, as shown in figure 14(*c*). Between $tu_\infty/L_c = 0$ and 0.21 (instant i), the spanwise vortices from shear layer roll-up, as observed in figure 7(*b*), give rise to the low amplitude pressure fluctuations travelling downstream, as shown in figure 14(*c*). These rollers merge at instant

https://doi.org/10.1017/jfm.2025.11019 Published online by Cambridge University Press

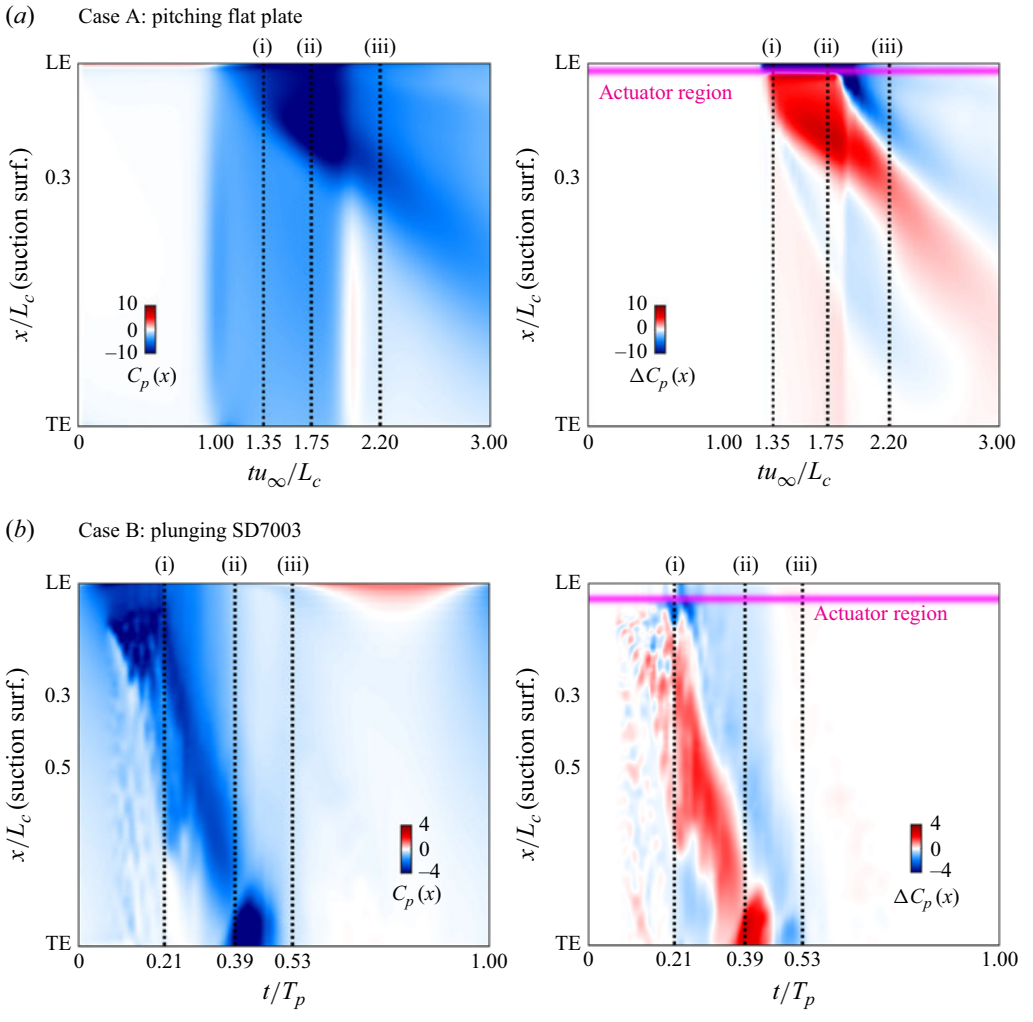


Figure 14. The evolution of suction-surface pressure distribution, $C_p(x) = (p(x) - p_\infty)/0.5\rho_\infty u_\infty^2$, for the baseline flows and the difference in the distribution between the baseline and controlled flows for case A (*a,b*) and case B (*c,d*) is presented. Representative time instants indicated in figure 12 are marked along the horizontal axis in each panel. Note that the actuator over the suction surface is highlighted by a shaded magenta region for both cases in (*b*) and (*d*).

(i) and form the core of the DSV, which builds up strong suction over the region of $x/L_c < 0.3$. After this instant, the DSV convects over the suction surface at a lower speed than the spanwise rollers observed in $tu_\infty/L_c = [0, 0.21]$, as indicated by the dark blue region in figure 14(*c*). Under the influence of control, we again observe pressure recovery starting from instant (i), due to the delayed formation of the DSV. Moreover, the reduced suction over the region $x/L_c > 0.5$ during $t/T_p \in [0.21, 0.39]$ reflects the diminished impact of the DSV in the controlled flow compared with baseline. Note here that for $t/T_p \in [0.21, 0.39]$, there is an enhanced suction for $x/L_c < 0.5$, which is due to the delayed presence of the DSV. However, the overall change in pressure distribution is favourable, resulting in the reduced lift fluctuation observed in figure 12.

Recall that the objective function of the broadcast mode analysis is to reduce circulation injection during the shedding of LEVs. Here, we analyse the physical flows obtained

https://doi.org/10.1017/jfm.2025.11019 Published online by Cambridge University Press

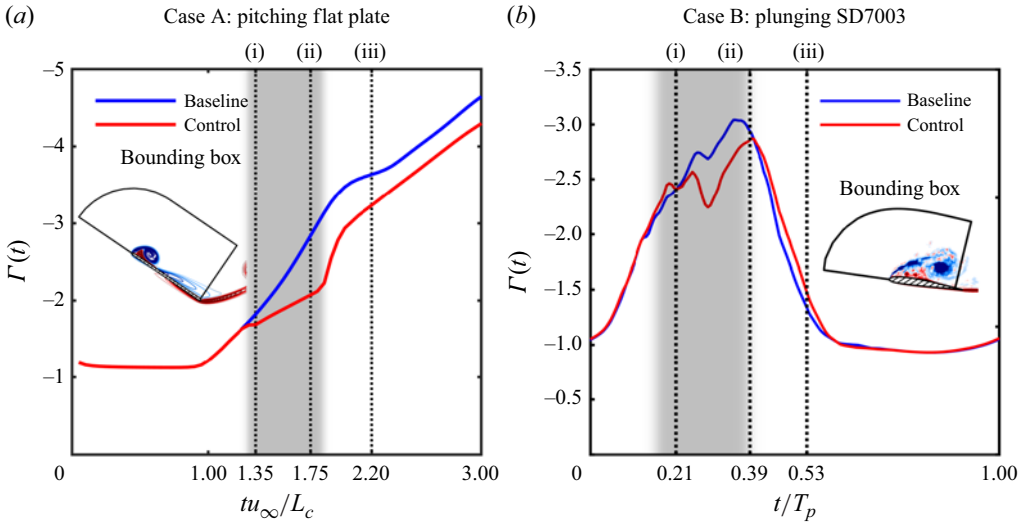


Figure 15. The temporal evolution of negative vorticity within the bounding box for both the baseline and control flows in cases A and B. The bounding boxes are chosen such that the entire suction surfaces of the aerofoils are covered.

from the LES to show that this objective is indeed achieved through the model-informed flow control. Following Visbal & Garmann (2018), we quantify the vorticity injection that forms the DSV by integrating the negative vorticity within a chosen bounding box. This is computed via

$$\Gamma(t) = \int_{\boldsymbol{x} \in bounding\ box} \omega_z^*(\boldsymbol{x}, t) \mathrm{d}v(\boldsymbol{x}), \tag{4.5}$$

where ω_z^* represents negative spanwise vorticity that characterises the DSV. A higher negative value of $\Gamma(t)$ indicates higher levels of negative vorticity introduced into the bounding box, which can be attributed to a stronger DSV.

The modifications in $\Gamma(t)$ and the choices of the bounding boxes for both cases are shown in figure 15. We observe significantly decreased vorticity injection in the controlled flows for both cases. For the baseline flow in case A, the non-zero vorticity within the bounding box is observed prior to the onset of pitching at $tu_\infty/L_c < 1$. This is primarily due to the presence of the boundary layer along the aerofoil surface. Following the initiation of pitching at $tu_\infty/L_c = 1$, the amount of negative vorticity within the bounding box increases due to accumulation of vorticity within the bounding box to form the DSV core. This is similar to the observations in figure 12(*a*), where the shear layer continuously feeds negative vorticity into the DSV. With the model-informed control, a reduction in $\Gamma(t)$ is observed at $tu_\infty/L_c = 1.35$ for case A. This is marked as instant (i) in figure 12(*a*), which is the same instant in figure 7(*a*) that marks the initiation of the DSV core formation in the baseline flow. The reduction in $\Gamma(t)$ becomes more pronounced at $tu_\infty/L_c = 1.75$, marked as instant (ii), where the lift reaches its peak in the baseline flow. At this instant, a 26 % reduction in vorticity within the bounding box is observed, suggesting that the reduction in lift fluctuation (shown in figure 14*b*) is attributed to a weakened DSV in the controlled flow, agreeing with the objective of the broadcast mode analysis.

For case B presented by figure 15(*b*), we observe a similar reduction in the vorticity content within the bounding box but of a different control mechanism. For instant (i) at

https://doi.org/10.1017/jfm.2025.11019 Published online by Cambridge University Press

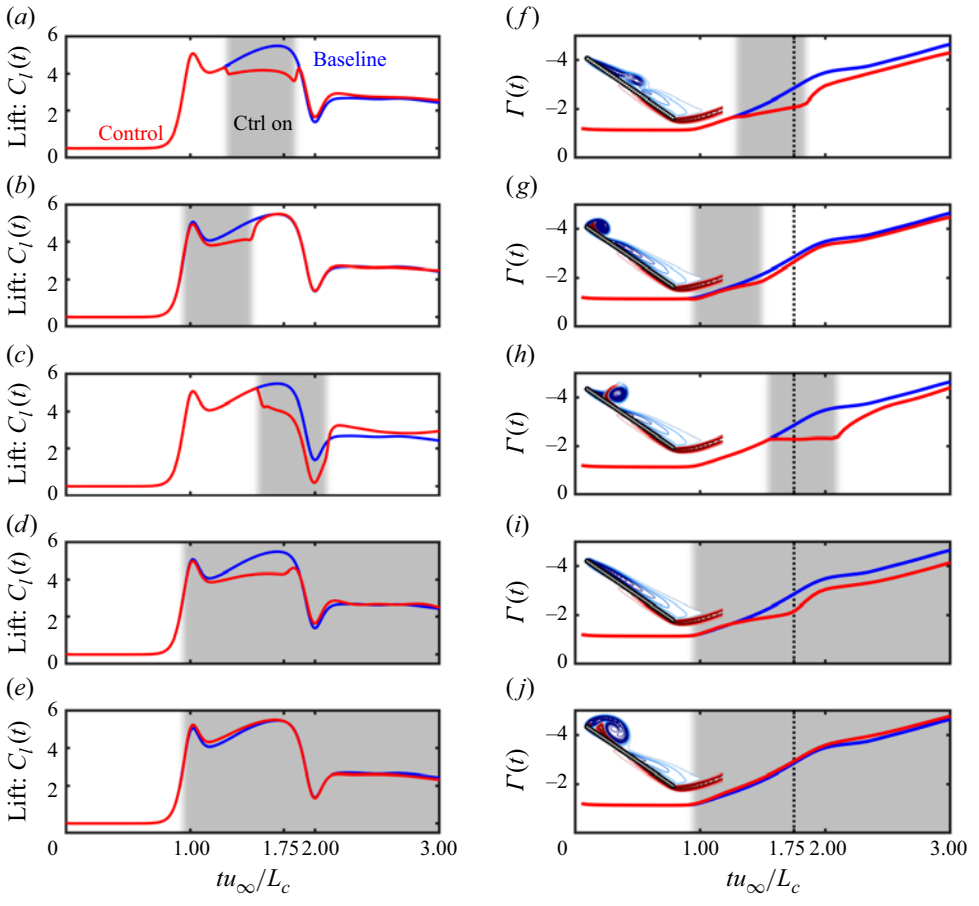


Figure 16. The time histories of the lift coefficient for the case of the pitching flat plate aerofoil (case A) are presented for five actuation cases: (*a*) actuation at the optimal time, $tu_\infty/L_c = 1.35$; (*b*) early actuation at $tu_\infty/L_c = 1$; (*c*) delayed actuation at $tu_\infty/L_c = 1.5$; (*d*) wall-normal suction; (*e*) wall-normal blowing. The corresponding time histories of negative circulation in the flow are shown in (*f*), (*g*), (*h*), (*i*) and (*j*), respectively, along with the spanwise vorticity field at $tu_\infty/L_c = 1.75$ for each case.

$t/T_p = 0.21$, the control input does not result in a notable decrease in $\Gamma(t)$. However, the small spanwise rollers in the controlled flow continue to travel along the suction surface without immediately merging near the leading edge to form the DSV core. This leads to a rapid decrease in $\Gamma(t)$ past $t/T_p = 0.21$. The formation of the DSV is delayed in the controlled flow for instant (ii), where we observe a significant decrease in $\Gamma(t)$ within the bounding box over $t/T_p \in [0.21, 0.35]$. The weaker DSV formed in the controlled flow suggests a lower injection of negative vorticity, which is also consistent with the objective of the broadcast mode analysis of the vortical network.

Furthermore, we consider in figure 16 three different timings to turn on the control inputs to highlight the effectiveness of the model-guided flow control. Here, we focus on the case of 2-D flow over a pitching flat plate (case A). In addition to the optimal timing guided by the broadcast mode analysis ($tu_\infty/L_c = 1.35$, figures 16*a* and 16*f*), LES of controlled flows are also performed with an early actuation at the beginning of pitching ($tu_\infty/L_c = 1$, figures 16*b* and 16*g*) and a delayed actuation when the aerofoil is midway through its pitching motion ($tu_\infty/L_c = 1.5$, figures 16*c* and 16*h*). For these three cases, we examine

https://doi.org/10.1017/jfm.2025.11019 Published online by Cambridge University Press

the control effects by comparing their lift fluctuations (figure 16*a–c*) and the circulations in the bounding box (figure 16*f–h*) to those in the baseline flow. Flow visualisations using the vorticity field at the instant $tu_\infty/L_c = 1.75$, where the baseline flow exhibits peak lift, are also inserted in figure 16(*f–h*) for comparison.

Compared with the case of optimal timing for actuation, the cases with both early and delayed actuation exhibit suboptimal control effects with respect to the reduction of lift fluctuation. For the case with early actuation, the lift recovers to the same level as that in the baseline flow after the control input is turned off. This case exhibits the smallest reduction in circulation within the bounding box among the three cases at $tu_\infty/L_c = 1.75$ and, as a result, fails to disrupt the formation of the DSV and consequently to reduce the peak lift. These observations are consistent with the insights from the broadcast mode analysis, which indicates that perturbing the vortices prior to the optimal time of $tu_\infty/L_c = 1.35$ has minimal effect on reducing the LEV strengths and, consequently, the development of the DSV. On the other hand, for the case with delayed actuation, the initial formation of the DSV was not interfered. Instead, the delayed control input prevents the shear layer from continuously feeding vorticity into the DSV, leading to the earlier departure of the DSV compared with the other two cases. Comparing this case with the optimal one, although the same levels of lift reduction are observed at $tu_\infty/L_c = 1.75$, the lift increase in the early stage of DSV formation is not circumvented and results in suboptimal control effectiveness in terms of peak lift. Overall, we observe that the case with optimal timing not only achieves high reduction in peak lift, but the circulation in the bounding box at $tu_\infty/L_c = 3$ as the DSV convects away is also the lowest among the three cases.

Let us consider two more actuation strategies in figure 16 to highlight the effectiveness of the model-guided flow control. In figures 16(*d*) and 16(*e*), respectively, wall-normal suction and wall-normal blowing are considered, since their uses have been widely examined for dynamic stall control in prior studies (McCloud, Hall & Brady 1960; Karim & Acharya 1994; Alrefai & Acharya 1996; Atik *et al.* 2005; Gardner *et al.* 2014; Müller-Vahl *et al.* 2016). For these two cases, the flow actuation begins at the onset of pitching ($tu_\infty/L_c = 1$) and continues until $tu_\infty/L_c = 3$. Here, the momentum coefficient is fixed at $C_\mu = 5.5\,\%$ across all cases. The cases of wall-normal suction and blowing exhibit suboptimal control effects relative to the network-guided strategy in reducing lift fluctuations (figure 16). For wall-normal suction (figures 16*d* and 16*i*), the reduction in peak lift coefficient is less pronounced than in the network-guided case. Although suction delays the formation of the DSV at $tu_\infty/L_c = 1.75$ (figure 16*i*), the injection of negative vorticity into the flow is slightly higher compared with the network-guided actuation. The case of wall-normal blowing produces the weakest modification to the peak lift coefficient (figure 16*e*) and allows a DSV to form near the leading edge at $tu_\infty/L_c = 1.75$, as in figure 16(*j*). Collectively, these results show that the network-guided actuation achieves a more effective reduction in peak lift by suppressing circulation injection. This outcome further supports the use of broadcast mode analysis for designing flow control strategies for dynamic stall.

The broadcast mode analysis was designed to reduce the strength of LEVs. Its results motivate us to target the flow near the leading edge at the critical instants associated with the shear layer pinch-up. The receiving mode revealed that the circulation of LEVs residing in the DSV core at later times can be reduced. For both cases considered, a reduction in peak lift is observed in the LES of controlled flows, as shown in figure 12. This results from the reduction in the suction induced by the DSV, as in figure 14, attributed to the formation of a weaker vortex core from reduced injection of negative vorticity, as confirmed by figure 15. These observations are in strong agreement with predictions from the network-based analysis of discrete vortices.

https://doi.org/10.1017/jfm.2025.11019 Published online by Cambridge University Press

5. Conclusions

We performed broadcast mode analysis of the vortical networks arising from dynamic stall flows to identify the optimal actuation location, timing and direction for suppressing the dynamic stall. This approach is demonstrated on two flows: a 2-D flow over a flat plate aerofoil at $Re = 1000$ and a heaving-plunging spanwise-periodic 3-D turbulent flow over an SD7003 aerofoil at $Re = 60\,000$. The framework leverages the time varying free-vortex states obtained from the DVM to understand the evolution of displacement perturbations to influence the circulation strength of LEVs within the vortical network. The broadcast mode analysis is reformulated as an optimisation problem that seeks the effective vortical nodes and the optimal timing in reducing the circulation strength of LEVs, with the objective of mitigating dynamic stall. The results of the analysis showed that the vortical nodes along the shear layer are the most effective nodes that appear at the instant of shear layer pinch-up. The analysis also showed that the broadcast mode based perturbation obtained from the optimal timing propagates to the vortical nodes residing in the DSV core at a later time. These insights from the broadcast mode analysis are used to inform the choice of actuator location, timing and direction in the simulation.

To validate the effectiveness of the network-guided actuation strategy, we implemented an actuator positioned near the leading edge in the LES and activated it at the optimal timing in the direction suggested by the network analysis. Simulation results show a significant reduction in peak lift by 21 % for the 2-D flows over the pitching flat plate aerofoil and 14 % for the 3-D turbulent flow over the plunging SD7003 aerofoil. The effect of flow control is found to modulate the negative vorticity injection into the DSV, consistent with the prediction of the broadcast mode analysis that the vortices within the DSV core are affected by vortical perturbations.

Lastly, we also note that the accuracy of the present broadcast mode analysis can be limited by that of the DVM employed in the present study (Ramesh *et al.* 2014; Lee *et al.* 2022). We observed discrepancies in the lift coefficient and the departure of the DSV. These discrepancies could be attributed to the thin-aerofoil theory adopted by the DVM, wherein the aerofoil is represented by a distribution of BVs along the camber line. Such an assumption can be inaccurate for aerofoils with finite thickness, and the results can be potentially improved by representing the aerofoil surface with discrete vortex panels (Morino & Kuo 1974; Katz 1981; Zhu *et al.* 2002; Xia & Mohseni 2017). The discrepancies could also be attributed to the setting that the critical leading-edge suction parameter was held constant in the present DVM. In such a case, potential improvements can be made by considering a time-varying critical leading-edge suction parameter, which has been shown to be more capable of capturing unsteady separation dynamics over aerofoils (Darakananda *et al.* 2018; Narsipur *et al.* 2020, 2023). Although improvement of the present DVM is possible, it reasonably captures the onset of DSV core formation and provides a simple yet practical framework for constructing a network-based model for the design of flow control. Its insights were also supported by the results of nonlinear simulations of controlled flows, demonstrating its capability to inform actuation strategies for dynamic stall mitigation.

In summary, the broadcast mode analysis guided flow control successfully reduced the lift fluctuation for both cases. This underscores the effectiveness of the network-based approach for determining the actuator location, timing and direction for dynamic stall mitigation by targeting the vorticity injection into the DSV. This study establishes a robust framework for active flow control design in the context of unsteady and transient flow separation, highlighting the potential of network-based analysis for flow control design.

https://doi.org/10.1017/jfm.2025.11019 Published online by Cambridge University Press

Acknowledgements. We are grateful for the support given by the Army Research Office (W911NF-23-1-0109), monitored by program managers Drs Joseph Myers, Jack Edwards, and Kenneth Granlund. We acknowledge the computing resources provided by North Carolina State University High Performance Computing Services Core Facility. The 3-D turbulent flow simulations were performed using computational resources sponsored by the Department of Energy's Office of Energy Efficiency and Renewable Energy and located at the National Renewable Energy Laboratory.

Declaration of interests. The authors report no conflict of interest.

Appendix A. Solver and mesh set-up

We used the incompressible flow solver in the CharLES software package to simulate the flow in a body-fixed non-inertial reference frame. The solver solves the incompressible Navier–Stokes equations that write

$$\boldsymbol{\nabla} \cdot \boldsymbol{u} = 0, \tag{A1}$$

$$\frac{\partial \boldsymbol{u}}{\partial t} + (\boldsymbol{u} \cdot \boldsymbol{\nabla})\boldsymbol{u} = -\boldsymbol{\nabla} p + 2\boldsymbol{\nabla} \cdot \left[(\nu + \nu_t)\, \boldsymbol{S}\right] + \boldsymbol{f}, \tag{A2}$$

where the fictitious forcing term $\boldsymbol{f}$ introduced for the non-inertial body-fixed reference (Agarwal & Deese 1987; Beddhu, Taylor & Whitfield 1996; Kim & Choi 2006) frame writes

$$\boldsymbol{f} = -2\dot{\alpha}(t) \times \boldsymbol{u} - \ddot{\alpha}(t) \times \boldsymbol{x} - \dot{\alpha}(t) \times (\dot{\alpha}(t) \times \boldsymbol{x}) - \ddot{h}(t). \tag{A3}$$

Here, $\boldsymbol{u}$ denotes the fluid velocity relative to the non-inertial body-fixed reference frame, p is the pressure, ν and ν_t are respectively the reference viscosity and the subgrid-scale (SGS) eddy viscosity, $\boldsymbol{S} \equiv (1/2)[\boldsymbol{\nabla u} + (\boldsymbol{\nabla u})^T]$ is the strain rate tensor and $\boldsymbol{x}$ is the position vector of the non-inertial body-fixed reference frame. The boundary condition imposed on the aerofoil is a no-slip condition. At the far field, the free-stream velocity is prescribed as

$$\boldsymbol{u} = -\dot{h}(t) - \dot{\alpha}(t) \times \boldsymbol{x}. \tag{A4}$$

For case A, 2-D simulations of flow around the flat plate aerofoil were performed by setting the SGS eddy viscosity to zero. An O-shaped computational grid, shown in figure 17(*a*), was employed with the plate pivoted about its leading edge, located at $(x/L_c, y/L_c) = (0, 0)$. The computational domain extends over $x/L_c, y/L_c \in [-30, 30]$ in both the streamwise and transverse directions. The mesh was designed such that the first-cell thickness is $\Delta y/L_c = 1 \times 10^{-3}$, containing approximately 5.5×10^5 grid nodes. Validation of the solver and mesh configuration was performed by comparing the lift coefficients obtained from CharLES with the numerical results of Ramesh *et al.* (2014), as shown in figure 2(*a*).

For case B, 3-D LES were performed on the computational grid shown in figure 17(*b*). In this case, we used Vreman's SGS model to calculate the SGS eddy viscosity ν_t (Vreman 2004). The SD7003 aerofoil is positioned such that its leading edge is located at $(x/L_c, y/L_c) = (0, 0)$. The computational domain extends over $x/L_c, y/L_c \in [-20, 20]$ in the streamwise and transverse directions, and $z/L_c \in [0, 0.4]$ in the spanwise direction. The mesh was designed with a first-cell thickness of $\Delta x/L_c = 2.5 \times 10^{-3}$, $\Delta y/L_c = 2.5 \times 10^{-4}$ and $\Delta z/L_c = 1 \times 10^{-2}$, resulting in approximately 3 million mesh nodes. Validation of the solver and mesh setting for case B is performed by comparing the lift coefficient obtained from CharLES with the numerical results of Visbal (2011), as shown in figure 2(*b*).

https://doi.org/10.1017/jfm.2025.11019 Published online by Cambridge University Press

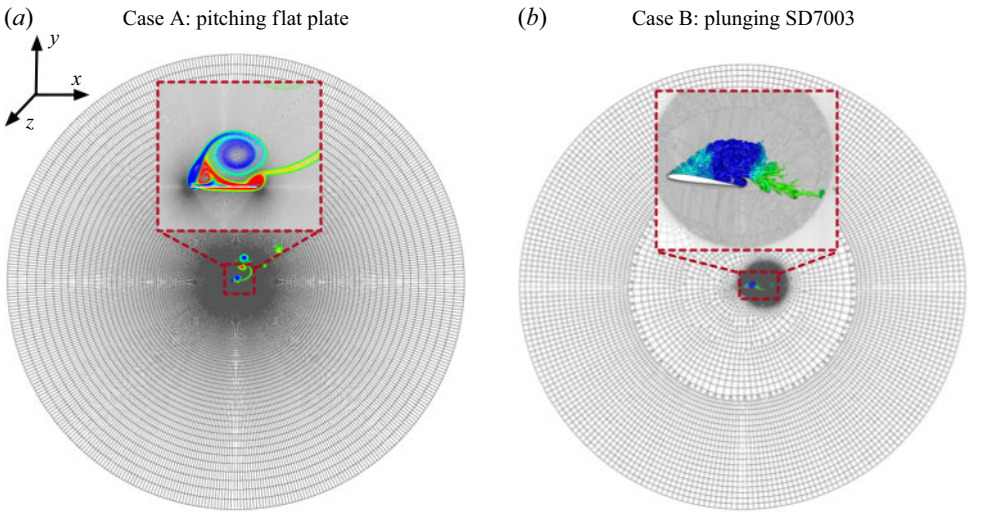


Figure 17. Computational meshes for (*a*) the pitching flat plate and (*b*) the periodically heaving-plunging SD7003 aerofoil is presented. For the flat plate aerofoil, the near-field mesh is shown together with the instantaneous spanwise vorticity field. For the SD7003 aerofoil, the near-field mesh is shown with an isosurface of the instantaneous Q criterion, coloured by pressure.

References

Agarwal, R.K. & Deese, J.E. 1987 Euler calculations for flowfield of a helicopter rotor in hover. *J. Aircraft* **24** (4), 231–238.

Albert, R. & Barabási, A.-L. 2002 Statistical mechanics of complex networks. *Rev. Mod. Phys.* **74** (1), 47–97.

Alrefai, M. & Acharya, M. 1996 Controlled leading-edge suction for management of unsteady separation over pitching airfoils. *AIAA J.* **34** (11), 2327–2336.

Alvarez, E.J. & Ning, A. 2020 High-fidelity modeling of multirotor aerodynamic interactions for aircraft design. *AIAA J.* **58** (10), 4385–4400.

Anderson, J.D. 2016 *Fundamentals of Aerodynamics*. McGraw hill.

Ansari, S.A., Żbikowski, R. & Knowles, K. 2006 Non-linear unsteady aerodynamic model for insect-like flapping wings in the hover. Part 2: implementation and validation. *Proc. Inst. Mech. Engrs G: J. Aerosp. Engng* **220** (3), 169–186.

Atik, H., Kim, C.-Y., Van Dommelen, L.L. & Walker, J.D.A. 2005 Boundary-layer separation control on a thin airfoil using local suction. *J. Fluid Mech.* **535**, 415–443.

Bai, Z., Erichson, N.B., Meena, M.G., Taira, K. & Brunton, S.L. 2019 Randomized methods to characterize large-scale vortical flow networks. *PLOS One* **14** (11), 1–19.

Beddhu, M., Taylor, L.K. & Whitfield, D.L. 1996 Strong conservative form of the incompressible Navier–Stokes equations in a rotating frame with a solution procedure. *J. Comput. Phys.* **128** (2), 427–437.

Brès, G.A., Ham, F., Nichols, J. & Lele, S. 2017 Unstructured large-eddy simulations of supersonic jets. *AIAA J.* **55** (4), 1164–1184.

Carr, L.W. 1988 Progress in analysis and prediction of dynamic stall. *J. Aircraft* **25** (1), 6–17.

Carr, L.W., McAlister, K.W. & McCroskey, W.J. 1977 Analysis of the development of dynamic stall based on oscillating airfoil experiments, *Tech. Rep.* A-6674. National Aeronautics and Space Administration.

Cattafesta III L.N. & Sheplak, M. 2011 Actuators for active flow control. *Annu. Rev. Fluid Mech.* **43** (1), 247–272.

Chen, W.-L., Li, H. & Hu, H. 2014 An experimental study on a suction flow control method to reduce the unsteadiness of the wind loads acting on a circular cylinder. *Exp. Fluids* **55**, 1–20.

Clements, R.R. 1973 An inviscid model of two-dimensional vortex shedding. *J. Fluid Mech.* **57** (2), 321–336.

Corke, T.C. & Thomas, F.O. 2015 Dynamic stall in pitching airfoils: aerodynamic damping and compressibility effects. *Annu. Rev. Fluid Mech.* **47**, 479–505.

https://doi.org/10.1017/jfm.2025.11019 Published online by Cambridge University Press

COTTET, G.-H. & KOUMOUTSAKOS, P.D. 2000 *Vortex Methods: Theory and Practice*. Cambridge University Press.

DARAKANANDA, D., ELDREDGE, J.D., DA SILVA, A., COLONIUS, T. & WILLIAMS, D.R. 2018 EnKF-based dynamic estimation of separated flows with a low-order vortex model. In *2018 AIAA Aerospace Sciences Meeting*, pp. 0811. American Institute of Aeronautics and Astronautics.

DARAKANANDA, D. & ELDREDGE, J.D. 2019 A versatile taxonomy of low-dimensional vortex models for unsteady aerodynamics. *J. Fluid Mech.* **858**, 917–948.

DE, S., GUPTA, S., UNNI, V.R., RAVINDRAN, R., KASTHURI, P., MARWAN, N., KURTHS, J. & SUJITH, R.I. 2023 Study of interaction and complete merging of binary cyclones using complex networks. *Chaos: Interdiscip. J. Nonlinear Sci.* **33** (1), 013129.

DUMOULIN, D., ELDREDGE, J.D. & CHATELAIN, P. 2023 A lightweight vortex model for unsteady motion of airfoils. *J. Fluid Mech.* **977**, A22.

ELDREDGE, J., WANG, C. & MICHAEL, O.L. 2009 A computational study of a canonical pitch-up, pitch-down wing maneuver. In *39th AIAA Fluid Dynamics Conference*, pp. 3687. American Institute of Aeronautics and Astronautics.

ELDREDGE, J.D. 2007 Numerical simulation of the fluid dynamics of 2D rigid body motion with the vortex particle method. *J. Comput. Phys.* **221** (2), 626–648.

ELDREDGE, J.D. & JONES, A.R. 2019 Leading-edge vortices: mechanics and modeling. *Annu. Rev. Fluid Mech.* **51** (1), 75–104.

FESZTY, D., GILLIES, E.A. & VEZZA, M. 2004 Alleviation of airfoil dynamic stall moments via trailing-edge flap flow control. *AIAA J.* **42** (1), 17–25.

GARDNER, A.D., JONES, A.R., MULLENERS, K., NAUGHTON, J.W. & SMITH, M.J. 2023 Review of rotating wing dynamic stall: experiments and flow control. *Prog. Aerosp. Sci.* **137**, 100887.

GARDNER, A.D., OPITZ, S., WOLF, C.C. & MERZ, C.B. 2017 Reduction of dynamic stall using a back-flow flap. *CEAS Aeronaut. J.* **8** (2), 271–286.

GARDNER, A.D., RICHTER, K., MAI, H. & NEUHAUS, D. 2014 Experimental investigation of high-pressure pulsed blowing for dynamic stall control. *CEAS Aeronaut. J.* **5** (2), 185–198.

GODAVARTHI, V., KAWAMURA, Y. & TAIRA, K. 2023 Optimal waveform for fast synchronization of airfoil wakes. *J. Fluid Mech.* **976**, R1.

GREENBLATT, D. & WYGNANSKI, I. 2001 Dynamic stall control by periodic excitation, part 1: NACA 0015 parametric study. *J. Aircraft* **38** (3), 430–438.

GRINDROD, P. & HIGHAM, D.J. 2013 A matrix iteration for dynamic network summaries. *SIAM Rev.* **55** (1), 118–128.

GRINDROD, P. & HIGHAM, D.J. 2014 A dynamical systems view of network centrality. *Proc. R. Soc. A Math. Phys. Engng Sci.* **470** (2165), 20130835.

GRINDROD, P., PARSONS, M.C., HIGHAM, D.J. & ESTRADA, E. 2011 Communicability across evolving networks. *Phys. Rev. E* **83** (4), 046120.

HERNDON, M.A. & JAWORSKI, J.W. 2023 Linear stability of a counter-rotating vortex pair approaching an inviscid wall. *Theor. Comput. Fluid Dyn.* **37** (4), 519–532.

IACOBELLO, G., KAISER, F. & RIVAL, D.E. 2022 Load estimation in unsteady flows from sparse pressure measurements: application of transition networks to experimental data. *Phys. Fluids* **34** (2), 025105.

IACOBELLO, G., RIDOLFI, L. & SCARSOGLIO, S. 2021 A review on turbulent and vortical flow analyses via complex networks. *Phys. A: Stat. Mech. Appl.* **563**, 125476.

IACOBELLO, G., SCARSOGLIO, S., KUERTEN, J.G.M. & RIDOLFI, L. 2019 Lagrangian network analysis of turbulent mixing. *J. Fluid Mech.* **865**, 546–562.

JOVANOVIĆ, M.R. 2004 Modeling, analysis, and control of spatially distributed systems. PhD thesis, University of California at Santa Barbara, Dept. of Mechanical Engineering, California, USA.

KAISER, E., NOACK, B.R., CORDIER, L., SPOHN, A., SEGOND, M., ABEL, M., DAVILLER, G., ÖSTH, J., KRAJNOVIĆ, S. & NIVEN, R.K. 2014 Cluster-based reduced-order modelling of a mixing layer. *J. Fluid Mech.* **754**, 365–414.

KARIM, M.A. & ACHARYA, M. 1994 Suppression of dynamic-stall vortices over pitching airfoils by leading-edge suction. *AIAA J.* **32** (8), 1647–1655.

KATZ, J. 1981 A discrete vortex method for the non-steady separated flow over an airfoil. *J. Fluid Mech.* **102**, 315–328.

KHALIGHI, Y., HAM, F., NICHOLS, J., LELE, S. & MOIN, P. 2011 Unstructured large eddy simulation for prediction of noise issued from turbulent jets in various configurations. In *17th AIAA/CEAS Aeroacoustics Conference (32nd AIAA Aeroacoustics Conference)*. American Institute of Aeronautics and Astronautics.

KIM, D. & CHOI, H. 2006 Immersed boundary method for flow around an arbitrarily moving body. *J. Comput. Phys.* **212** (2), 662–680.

https://doi.org/10.1017/jfm.2025.11019 Published online by Cambridge University Press

KISSING, J., KRIEGSEIS, J., LI, Z., FENG, L., HUSSONG, J. & TROPEA, C. 2020 Insights into leading edge vortex formation and detachment on a pitching and plunging flat plate. *Exp. Fluids* **61**, 1–18.

KISSING, J., STUMPF, B., KRIEGSEIS, J., HUSSONG, J. & TROPEA, C. 2021 Delaying leading edge vortex detachment by plasma flow control at topologically critical locations. *Phys. Rev. Fluids* **6** (2), 023101.

KOUMOUTSAKOS, P., LEONARD, A. & PEPIN, F. 1994 Boundary conditions for viscous vortex methods. *J. Comput. Phys.* **113** (1), 52–61.

LANDER, M. & HOLLAND, G.J. 1993 On the interaction of tropical-cyclone-scale vortices. I: observations. *Q. J. R. Meteorol. Soc.* **119** (514), 1347–1361.

LEE, Y.T., SURESH BABU, A.V., BRYANT, M. & GOPALARATHNAM, A. 2022 State variable form of unsteady airfoil aerodynamics with vortex shedding. In *AIAA SCITECH 2022 Forum*, pp. 1667. American Institute of Aeronautics and Astronautics.

LEISHMAN, J.G. 1990 Dynamic stall experiments on the NACA 23012 aerofoil. *Exp. Fluids* **9** (1), 49–58.

LI, H., FERNEX, D., SEMAAN, R., TAN, J., MORZYŃSKI, M. & NOACK, B.R. 2021 Cluster-based network model. *J. Fluid Mech.* **906**, A21.

LIN, C.-T., TSAI, M.-L. & TSAI, H.-C. 2023 Flow control of a plunging cylinder based on resolvent analysis. *J. Fluid Mech.* **967**, A41.

LOMBARDI, A.J., BOWLES, P.O. & CORKE, T.C. 2013 Closed-loop dynamic stall control using a plasma actuator. *AIAA J.* **51** (5), 1130–1141.

MCCLOUD, J.L., HALL, L.P. & BRADY, J.A. 1960 *Full Scale Wind-Tunnel Tests of Blowing Boundary-Layer Control Applied to a Helicopter Rotor*. National Aeronautics and Space Administration.

MCCROSKEY, W.J. 1981 The phenomenon of dynamic stall. *Tech. Rep.* A-8464. National Aeronautics and Space Administration.

MCCROSKEY, W.J., CARR, L.W. & MCALISTER, K.W. 1976 Dynamic stall experiments on oscillating airfoils. *AIAA J.* **14** (1), 57–63.

MEENA, M.G. & TAIRA, K. 2021 Identifying vortical network connectors for turbulent flow modification. *J. Fluid Mech.* **915**, A10.

MORINO, L. & KUO, C.-C. 1974 Subsonic potential aerodynamics for complex configurations: a general theory. *AIAA J.* **12** (2), 191–197.

MÜLLER-VAHL, H.F., NAYERI, C.N., PASCHEREIT, C.O. & GREENBLATT, D. 2016 Dynamic stall control via adaptive blowing. *Renew. Energy* **97**, 47–64.

NAIR, A.G. & TAIRA, K. 2015 Network-theoretic approach to sparsified discrete vortex dynamics. *J. Fluid Mech.* **768**, 549–571.

NAIR, A.G., TAIRA, K., BRUNTON, B.W. & BRUNTON, S.L. 2021 Phase-based control of periodic flows. *J. Fluid Mech.* **927**, A30.

NANDE, A., ADLAM, B., SHEEN, J., LEVY, M.Z. & HILL, A.L. 2021 Dynamics of COVID-19 under social distancing measures are driven by transmission network structure. *PLOS Comput. Biol.* **17** (2), e1008684.

NARSIPUR, S., HOSANGADI, P., GOPALARATHNAM, A. & EDWARDS, J.R. 2020 Variation of leading-edge suction during stall for unsteady aerofoil motions. *J. Fluid Mech.* **900**, A25.

NARSIPUR, S., RAMESH, K., GOPALARATHNAM, A. & EDWARDS, J.R. 2023 Discrete vortex modeling of perching and hovering maneuvers. *Theor. Comput. Fluid Dyn.* **37** (4), 445–464.

NATARAJAN, M., FREUND, J.B. & BODONY, D.J. 2016 Actuator selection and placement for localized feedback flow control. *J. Fluid Mech.* **809**, 775–792.

NEWMAN, M.E.J. 2010 *Networks: an Introduction*. Oxford Univ. Press.

POST, M.L. & CORKE, T.C. 2006 Separation control using plasma actuators: dynamic stall vortex control on oscillating airfoil. *AIAA J.* **44** (12), 3125–3135.

RAMESH, K., GOPALARATHNAM, A., GRANLUND, K., OL, M.V. & EDWARDS, J.R. 2014 Discrete-vortex method with novel shedding criterion for unsteady aerofoil flows with intermittent leading-edge vortex shedding. *J. Fluid Mech.* **751**, 500–538.

RAMOS, B.L.O., WOLF, W.R., YEH, C.-A. & TAIRA, K. 2019 Active flow control for drag reduction of a plunging airfoil under deep dynamic stall. *Phys. Rev. Fluids* **4** (7), 074603.

SAFARI, M., FLEMING, C., GALVIS, J.A., DEKA, A., MACHADO, G. & YEH, C.-A. 2025 A CFD-informed barn-level swine disease dissemination model and its use for ventilation optimization. *Epidemics-NETH* **51**, 100835.

SAFFMAN, P.G. 1995 *Vortex Dynamics*. Cambridge University Press.

SARPKAYA, T. 1975 An inviscid model of two-dimensional vortex shedding for transient and asymptotically steady separated flow over an inclined plate. *J. Fluid Mech.* **68** (1), 109–128.

SCHLOSSER, F., MAIER, B.F., JACK, O., HINRICHS, D., ZACHARIAE, A. & BROCKMANN, D. 2020 COVID-19 lockdown induces disease-mitigating structural changes in mobility networks. *Proc. Natl Acad. Sci. USA* **117** (52), 32883–32890.

https://doi.org/10.1017/jfm.2025.11019 Published online by Cambridge University Press

SINGH, C., PEAKE, D.J., KOKKALIS, A., KHODAGOLIAN, V., COTON, F.N. & GALBRAITH, R.A.M. 2006 Control of rotorcraft retreating blade stall using air-jet vortex generators. *J. Aircraft* **43** (4), 1169–1176.

DE SOUZA, L.F., WOLF, W.R., SAFARI, M. & YEH, C.-A. 2025 Control of deep dynamic stall by duty-cycle actuation informed by stability analysis. *AIAA J.* **63** (11), 1–12.

SUJITH, R.I. & UNNI, V.R. 2020 Complex system approach to investigate and mitigate thermoacoustic instability in turbulent combustors. *Phys. Fluids* **32** (6), 061401.

SURESHBABU, A., RAMESH, K. & GOPALARATHNAM, A. 2019 Model reduction in discrete-vortex methods for unsteady airfoil flows. *AIAA J.* **57** (4), 1409–1422.

TADJFAR, M. & ASGARI, E. 2018 The role of frequency and phase difference between the flow and the actuation signal of a tangential synthetic jet on dynamic stall flow control. *J. Fluids Engng* **140** (11), 111203.

TANDON, S. & SUJITH, R.I. 2023 Multilayer network analysis to study complex inter-subsystem interactions in a turbulent thermoacoustic system. *J. Fluid Mech.* **966**, A9.

VINCETI, M., FILIPPINI, T., ROTHMAN, K.J., FERRARI, F., GOFFI, A., MAFFEIS, G. & ORSINI, N. 2020 Lockdown timing and efficacy in controlling COVID-19 using mobile phone tracking. *EClinicalMedicine* **25**, 100457.

VISBAL, M.R. 2011 Numerical investigation of deep dynamic stall of a plunging airfoil. *AIAA J.* **49** (10), 2152–2170.

VISBAL, M.R. & GARMANN, D.J. 2018 Analysis of dynamic stall on a pitching airfoil using high-fidelity large-eddy simulations. *AIAA J.* **56** (1), 46–63.

VREMAN, A.W. 2004 An eddy-viscosity subgrid-scale model for turbulent shear flow: algebraic theory and applications. *Phys. Fluids* **16** (10), 3670–3681.

WANG, Z., ZHANG, G., SUN, T. & ZHOU, B. 2025 Development and application of a fluid mechanics analysis framework based on complex network theory. *Comput. Meth. Appl. Mech. Engng* **435**, 117677.

WEAVER, D., MCALISTER, K.W. & TSO, J. 2004 Control of VR-7 dynamic stall by strong steady blowing. *J. Aircraft* **41** (6), 1404–1413.

XIA, X. & MOHSENI, K. 2013 Lift evaluation of a two-dimensional pitching flat plate. *Phys. Fluids* **25** (9), 091901.

XIA, X. & MOHSENI, K. 2017 Unsteady aerodynamics and vortex-sheet formation of a two-dimensional airfoil. *J. Fluid Mech.* **830**, 439–478.

YEH, C.-A., BENTON, S.I., TAIRA, K. & GARMANN, D.J. 2020 Resolvent analysis of an airfoil laminar separation bubble at $\mathrm{Re} = 500\,000$. *Phys. Rev. Fluids* **5**, 083906.

YEH, C.-A., MEENA, M.G. & TAIRA, K. 2021 Network broadcast analysis and control of turbulent flows. *J. Fluid Mech.* **910**, A15.

ZHU, C., QIU, Y., FENG, Y., WANG, T. & LI, H. 2022 Combined effect of passive vortex generators and leading-edge roughness on dynamic stall of the wind turbine airfoil. *Energy Convers. Manage.* **251**, 115015.

ZHU, Q., WOLFGANG, M.J., YUE, D.K.P. & TRIANTAFYLLOU, M.S. 2002 Three-dimensional flow structures and vorticity control in fish-like swimming. *J. Fluid Mech.* **468**, 1–28.

ZIGUNOV, F., SELLAPPAN, P. & ALVI, F. 2022 A bluff body flow control experiment with distributed actuation and genetic algorithm-based optimization. *Exp. Fluids* **63** (1), 23.

https://doi.org/10.1017/jfm.2025.11019 Published online by Cambridge University Press